High-angle active conjugate faults in the Anza-Borrego shear zone, Southern California

Xiaoyu Zou[1], Yuri Fialko[2], Andrew Dennehy[3], Alexander Cloninger[4], and Shabnam Semnani[5]

[1]Institute of Geophysics and Planetary Physics, Scripps Institute of Oceanography, UC San Diego
[2]UCSD
[3]Committe on Computational and Applied Mathematics, University of Chicago
[4]Department of Mathematics & Halicioglu Data Science Institute, UC San Diego
[5]Department of Structural Engineering, UC San Diego

October 27, 2023

Abstract

Orientations of active antithetic faults can provide useful constraints on in situ strength of the seismogenic crust. We use LINSCAN, a new unsupervised learning algorithm for identifying quasi-linear clusters of earthquakes, to map small-scale strike-slip faults in the Anza-Borrego shear zone, Southern California. We identify 332 right- and left-lateral faults having lengths between 0.1-3 km. The dihedral angles between all possible pairs of conjugate faults are nearly normally distributed around 70 degrees, with a standard deviation of 30 degrees. The observed dihedral angles are larger than those expected assuming optimal fault orientations and the coefficient of friction of 0.6-0.8, but similar to the distribution previously reported for the Ridgecrest area in the Eastern California Shear Zone. We show that the observed fault orientations can be explained by fault rotation away from the principal shortening axis due to a cumulated tectonic strain.

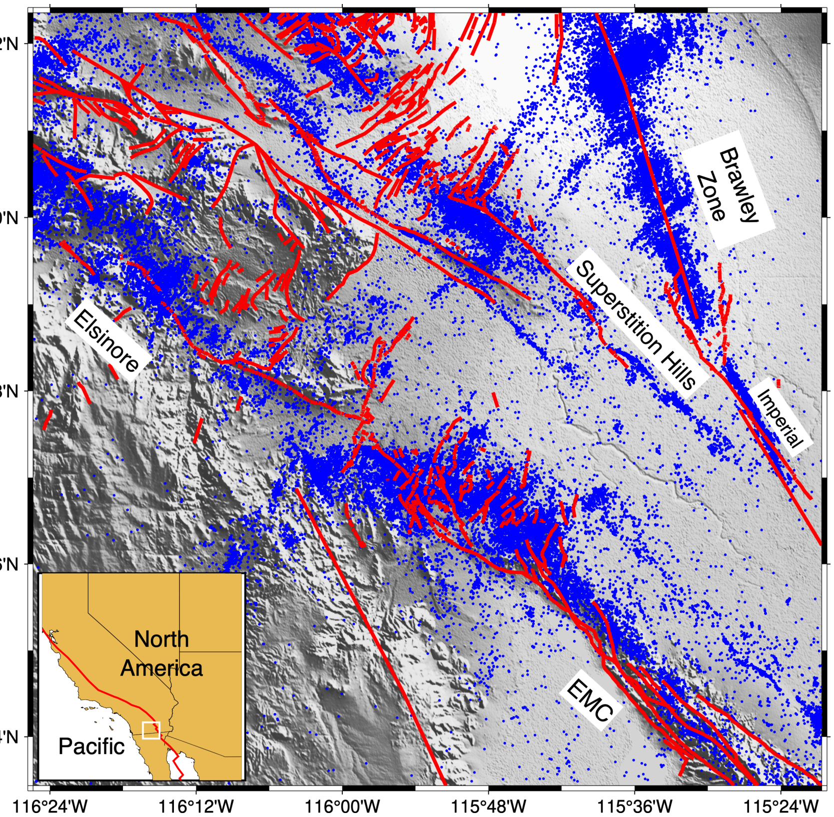

Figure 1: Map of the study area, with shaded relief. Red lines denote traces of Quaternary faults (Jennings & Bryant, 2010). Blue dots denote earthquake epicenters from Cheng et al. (2023) catalog. EMC="El Mayor-Cucapah". The inset shows the regional setting with respect to the North America-Pacific plate boundary (red line).

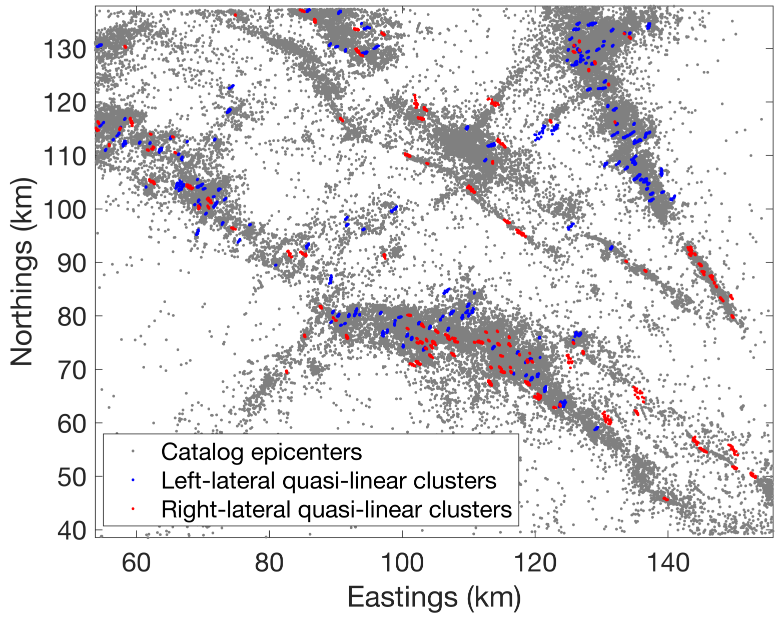

Figure 2: Grey dots: catalog epicenters (same as in Figure 1). Red and blue dots: quasi- linear clusters of epicenters with right- and left-lateral sense of slip, respectively, identified by our analysis. A total of 332 clusters are shown, including 195 left-lateral clusters and 137 right-lateral clusters. The minimum and maximum cluster lengths are 76 m and 3.05 km, respectively.

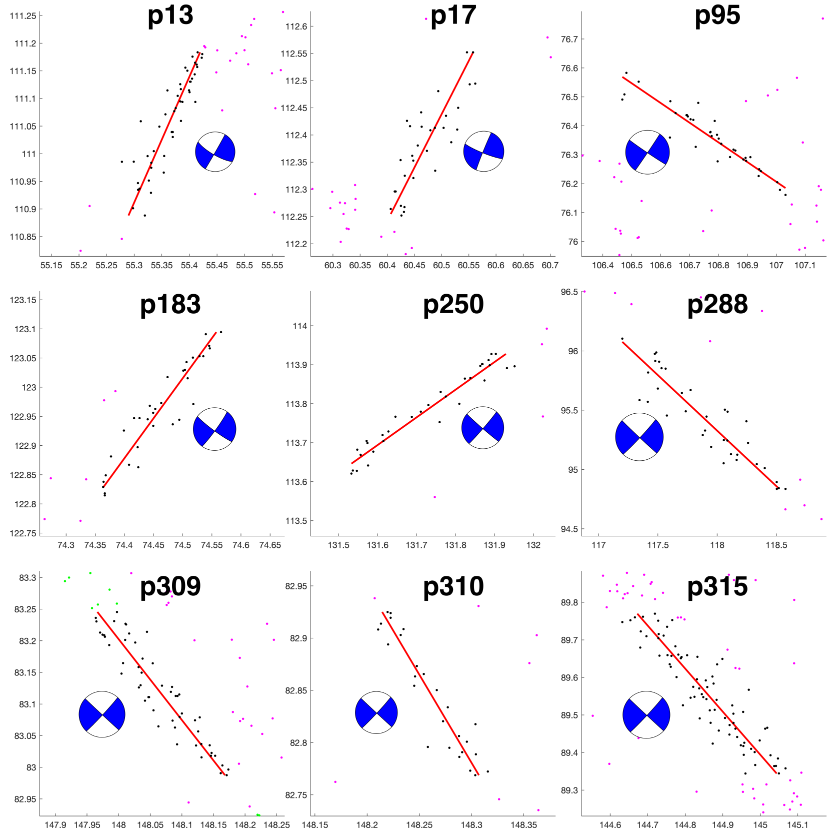

Figure 3: Examples of quasi-linear clusters (QLCs) that passed the quality control checks. Black dots denote earthquakes constituting a cluster, and magenta dots denote the background seismicity. Red lines denote best-fitting linear segments. Blue beach balls denote composite focal mechanisms. Numerical labels denote cluster numbers (see Supplementary Figures S5-S16). Axes represent northing and easting coordinates, in km.

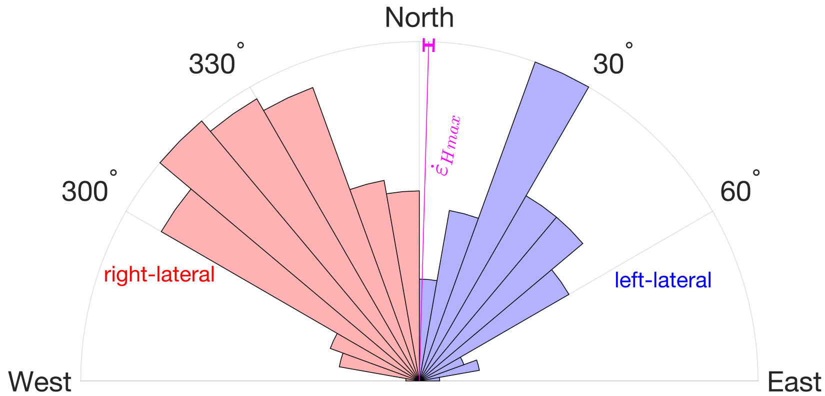

Figure 4: A distribution of strike angles of high-quality QLCs shown in Figures 3 and S4- S16. Red histogram corresponds to right-lateral faults (total of 137 samples), and blue histogram corresponds to left-lateral faults (total of 195 samples). Thin magenta line denotes the average orientation of the principal shortening rate axis (see Figure S3). The magenta error bar denotes 4 standard deviations.

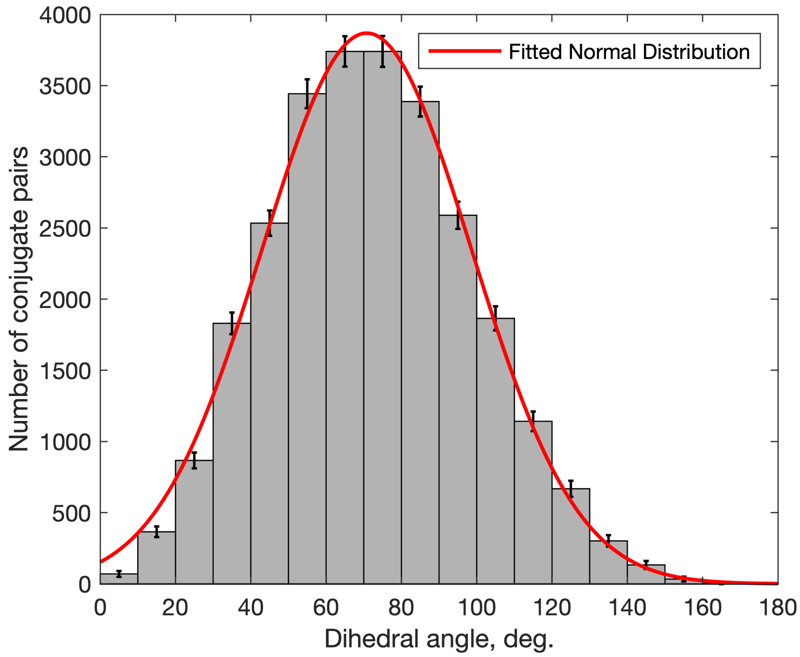

Figure 5: A histogram of dihedral angles between the conjugate strike-slip faults shown in Figure 4. Dihedral angles were computed between every possible pair of right- and left-lateral faults. Error bars denote 2σ uncertainty (see Fialko (2021) for details of the error analysis). The red curve denotes the best-fitting Gaussian distribution. The mean is 70.8 and the standard deviation is 28.9 degrees.

High-angle active conjugate faults in the Anza-Borrego shear zone, Southern California

Xiaoyu Zou[1], Yuri Fialko[1], Andrew Dennehy[2], Alexander Cloninger[3,4], Shabnam J. Semnani[5]

[1]Institute of Geophysics and Planetary Physics, Scripps Institution of Oceanography, University of California San Diego, La Jolla, CA 92093, USA.
[2]Committee on Computational and Applied Mathematics, University of Chicago, Chicago, IL 60615, USA.
[3]Department of Mathematical Sciences, University of California San Diego, La Jolla, CA 92093, USA.
[4]Halıcıoğlu Data Science Institute, University of California San Diego, La Jolla, CA 92093, USA
[5]Department of Structural Engineering, University of California San Diego, La Jolla, CA 92093, USA.

Key Points:

- We use a new algorithm to identify quasi-linear clusters of micro-earthquakes associated with active strike-slip faults in a trans-tensional region south of the Salton Sea, Southern California.
- The observed dihedral angles between right- and left-lateral faults show a broad distribution with a peak around 70°.
- Non-optimal fault orientations can be explained by tectonic rotation due to a long-term slip on a more mature system of right-lateral faults.

Corresponding author: Xiaoyu Zou, x3zou@ucsd.edu

Abstract

Orientations of active antithetic faults can provide useful constraints on in situ strength of the seismogenic crust. We use LINSCAN, a new unsupervised learning algorithm for identifying quasi-linear clusters of earthquakes, to map small-scale strike-slip faults in the Anza-Borrego shear zone, Southern California. We identify 332 right- and left-lateral faults having lengths between 0.1-3 km. The dihedral angles between all possible pairs of conjugate faults are nearly normally distributed around 70 degrees, with a standard deviation of ∼30 degrees. The observed dihedral angles are larger than those expected assuming optimal fault orientations and the coefficient of friction of 0.6-0.8, but similar to the distribution previously reported for the Ridgecrest area in the Eastern California Shear Zone. We show that the observed fault orientations can be explained by fault rotation away from the principal shortening axis due to a cumulated tectonic strain.

Plain Language Summary

Small earthquakes can highlight the location and attitude of active faults at depth. We use a large set of earthquake locations and a novel algorithm to identify small faults, along with their orientations, and sense of slip. We find that faults with opposite sense of slip (the so-called antithetic, or conjugate faults) are at nearly right angles to each other. For newly created faults, such a configuration would imply that friction is almost negligible. We suggest that the high-angle conjugate faults instead result from fault rotation due to long-term tectonic deformation.

Introduction

According to the Mohr-Coulomb failure theory, new or pre-existing faults should be preferentially activated at an angle $\pm\theta_0$ to the principal compression axis (Anderson, 1951; Sibson, 1974; Scholz, 2019). The two antithetic fault orientations are known as conjugate faults (e.g., Twiss & Moores, 1992, p. 141). For typical laboratory values of the static coefficient of friction μ of 0.6-0.8 (Byerlee, 1978), the dihedral angle between optimally oriented conjugate faults is $2\theta_0 = \arctan(\mu^{-1}) \approx 50 - 60$ degrees (Anderson, 1951; Sibson, 1974). While in some cases there is good agreement between predictions of the Mohr-Coulomb theory and the observed fault orientations (Walsh & Watterson, 1988; Alt & Zoback, 2017), there are also ample examples of conjugate faults that are not optimally oriented with respect to each other and/or the inferred principal stress axes, assuming the Byerlee's friction. In fact, many active conjugate faults exhibit dihedral angles close to 90 degrees, considerably greater than $2\theta_0$ (McGill et al., 1989; Thatcher & Hill, 1991; Yue et al., 2012; Jin & Fialko, 2020; Fialko & Jin, 2021; Hatch-Ibarra et al., 2022). Proposed explanations include anomalously low in situ friction (e.g., Middleton & Copley, 2014; Ross et al., 2019), a dominant control of deep fault roots in the ductile lower crust (Thatcher & Hill, 1991; Scholz & Choi, 2022; Liang et al., 2021), and fault rotation due to finite tectonic strain (Cloos, 1955; Freund, 1970; Nur et al., 1986; Fialko & Jin, 2021). A low frictional strength is often inferred in case of mature well-slipped faults (Mount & Suppe, 1987; Wernicke, 1995; Sibson, 1994), presumably due to activation of various weakening mechanisms (Rice, 2006; Di Toro et al., 2011; Brown & Fialko, 2012). However, the bulk of the seismogenic upper crust is unlikely extremely weak, as evidenced by optimal orientations of at least some active faults (Walsh & Watterson, 1988; Alt & Zoback, 2017), stress measurements in deep boreholes (Townend & Zoback, 2000), and long-term support of topography (Coblentz et al., 1994; Burov, 2011; Fialko et al., 2005). Deep ductile roots could possibly control the orientation of faults that originate at the bottom of the seismogenic zone and/or cut through the entire brittle crust (Scholz & Choi, 2022), but not of the abundant small faults having characteristic dimensions of less than $\sim$10 km that are unlikely connected to the ductile substrate (Fialko & Jin, 2021). It was also suggested that faults may typically form at near-optimal angles, but be subsequently rotated away from the axis of maximum compressive stress due to finite tectonic strain (Cloos, 1955; Freund, 1970; Fialko & Jin, 2021). The maximum rotation angle is limited by a fault lock-up, and is on the order of θ_0 (Nur et al., 1986; Sibson, 1990).

These hypotheses can be discriminated by quantifying relative orientations of small active faults. Fialko and Jin (2021) noted that lineated clusters of microseismicity in the Eastern California Shear Zone near Ridgecrest reveal multiple high-angle conjugate faults consistent with the rupture geometry of the M6.4 foreshock and M7.1 mainshock of the 2019 Ridgecrest earthquake sequence (Ross et al., 2019; Jin & Fialko, 2020; Fialko, 2021). Fialko and Jin (2021) further showed that the observed fault geometries are consistent with finite strain and rotation since the inception of the Eastern California Shear Zone. It is of interest to quantify relative orientations of conjugate faults in different regions undergoing active deformation (Fialko, 2021). However, identifying and systematically mapping active fault structures is a challenging task, especially in case of relatively small faults that typically do not have a surface expression.

In this paper, we apply a new algorithm to map out a population of active strike-slip faults in the Anza-Borrego shear zone in Southern California, and evaluate the distribution of dihedral angles between the identified sets of antithetic (i.e., left- and right-lateral) faults. We then use the observed fault orientations to evaluate possible controlling mechanisms.

1 Data and Methods

Active faults are often expressed in microseismicity (Valoroso et al., 2009; Nadeau & McEvilly, 1999). In case of strike-slip faults, the associated microearthquakes appear as localized streaks of epicenters in a map view (e.g., Alt & Zoback, 2017; Fialko, 2021). The respective quasi-linear clusters (QLCs) of events can be used to map active fault structures (Skoumal et al., 2019; Fialko, 2021). Several algorithms were proposed to identify lineated structures in highly scattered point clouds, all based on the point density and/or Euclidian distance between candidate points (Skoumal et al., 2019; Cochran et al., 2020; Fialko, 2021). In particular, Fialko (2021) used a non-parametric unsupervised learning algorithm OPTICS (Ordering Points To Identify the Clustering Structure; Ankerst et al., 1999), a variant of DBSCAN (Schubert et al., 2017), to separate clustered events from the background seismicity. One of the drawbacks of proximity-based algorithms such as OPTICS and DBSCAN is that the selected clusters can be of arbitrary shape, and additional screening is needed to cull out clusters having isometric or irregular geometries. Oftentimes such clusters contain smaller-scale lineated features that could be sensibly associated with active faults but would be missed by the search algorithm if the parental cluster is culled out. A robust procedure for multi-scale identification of quasi-linear sets of epicenters is therefore highly warranted.

1.1 LINSCAN Algorithm

We use LINSCAN, a new algorithm based on OPTICS, in which the Euclidean distance metric is replaced with a distance function $D(P, Q)$ derived from Kullback-Leibler (KL) divergence. The KL divergence is a measure of how similar two given distributions are. For two groups of points P and Q, the distance function $D(P, Q)$ is minimized when points in both groups are distributed along similar directions (see Supplementary Information for details). This ensures that only specific geometric shapes (in this case, QLCs) are selected. We evaluated the accuracy and robustness of the algorithm using a synthetic catalog of earthquake epicenters. The synthetic catalog consists of (i) arbitrarily oriented QLCs of various sizes, (ii) quasi-isometric clusters, and (iii) randomly distributed "background seismicity" (see Figure S1a in the Supplementary Information). The LINSCAN algorithm is able to efficiently identify and separate QLCs from the rest of the data (Figure S1b). Occasionally, some of the original QLCs are split into co-linear subsegments (Figure S1b). This is not a major issue since we are interested in accurate estimation of the fault strike angles. If needed, adjacent QLCs can be merged by considering their proximity and along-strike continuity. More importantly, the algorithm is able to identify overlapping and intersecting clusters that are ubiquitous in the case of complex fault systems (e.g., Fialko, 2021), although for some of the overlapping clusters the selection choices are non-unique. In the test shown in Figure S1, the number of points identified as belonging to QLCs (Figure S1b) is about 80% of the total number of "true" QLC points in the input data set (Figure S1a). A small fraction of points was identified as QLCs even though they did not belong to any of the input QLCs, due to either false detections or spontaneous quasi-linear patterns in the randomly generated "background seismicity".

1.2 Data analysis

We apply LINSCAN to quantify relative orientations of small strike-slip faults in a region of active deformation to the south of the Salton Sea, Southern California (Figure 1). This region accommodates $\sim$20 mm/yr of strike-slip motion between the North American and Pacific plates (Tymofyeyeva & Fialko, 2018), and hosts a number of active faults of various degrees of maturity (Jennings & Bryant, 2010), as well as abundant microseismicity (Yang & Hauksson, 2013). This region, hereafter referred to as the Anza-Borrego shear zone, is part of a transtensional transition zone connecting the Southern San Andreas Fault system to the Cerro Prieto fault system, and ultimately to the Gulf of California (Herzig & Jacobs, 1994; Crowell et al., 2013; Gonzalez-Ortega et al., 2014). We use a recently published catalog of precisely located events with focal mechanisms that spans 1981-2021 (Cheng et al., 2023). The event locations are shown in Figure 1. We convert geographic coordinates to the local Cartesian (UTM) coordinates using a local origin at 117°W, 32°N. The catalog epicenters and the QLCs selected by LINSCAN are shown in Figure S4 (blue and orange dots, respectively).

To ensure that the selected QLCs are robust, we perform several quality checks. As spurious linear patterns may emerge at the boundaries of the area of interest (due to the discarding of data outside of the bounding box), we removed all east-west and north-south striking clusters near the respective boundaries. For each "inside" cluster, we compute the Pearson correlation coefficient $r = \sum_i (x_i - \bar{x})(y_i - \bar{y}) / \sqrt{\sum_i (x_i - \bar{x})^2 \sum_i (y_i - \bar{y})}^2$, where x_i, y_i are coordinates (northings and eastings) of each epicenter, and $\bar{x}$, $\bar{y}$ are the means of x, y coordinates of events comprising a given cluster (e.g., Artusi et al., 2002). We retain clusters for which the absolute value of the correlation coefficient is greater or equal to 0.5. We further fit a straight line segment to the respective sets of points for each cluster, and compute the mean normalized distance δ between the points and the best-fit line as the mean of distances from the points to the line, divided by the line length. We discard clusters for which $\delta > 0.1$. Since we are interested in strike-slip faults, we discard clusters for which the dip angle of either P or T axis is greater than 40°. Finally, we perform a visual check to discard clusters in which the events are too sparse, unevenly distributed, hard to distinguish from the background seismicity, or organized in sub-clusters with significantly different orientations. Figure S2 shows several examples of the culled out "low quality" clusters, and Figures 3 and S5-S16 show QLCs that satisfy the above criteria. Out of the 1181 QLCs initially identified by LINSCAN (Figure S4), 332 QLCs passed the quality checks, and were used in the subsequent analysis.

To separate the sets of right- and left-lateral faults, for each QLC we compute composite focal mechanisms by summing up the moment tensors of individual events normalized by their scalar moments (Fialko, 2021). Given the fault plane (revealed by the QLC strike) and polarity of the composite focal mechanism, we determine the sense of slip on each identified fault. Consistent with the approximately north-south orientation of the principal strain rate axis (Figure S3), right-lateral faults strike predominantly north-west, and left-lateral faults strike predominantly north-east (Figure 4). Figure 2 shows the locations of the identified right- and left-lateral faults (red and blue dots, respectively). In total, there are 195 left-lateral faults and 137 right-lateral faults. The left-lateral faults have predominant strikes of ∼20-30°, and right-lateral faults strike between ∼300-340° (Figure 4). The dominant orientations of active faults shown in Figure 4 are consistent with orientations of the right- and left-lateral Quaternary fault traces in our study area

(Figure 1). The dihedral angles between the identified QLCs (Figure 2) are calculated by taking the difference in fault strikes for every possible pair of right- and left-lateral faults (Fialko, 2021). Figure 5 shows the resulting distribution of dihedral angles. Similar results are obtained when we limit the distance between conjugate faults to be less than 5 km, although the number of samples is substantially reduced.

2 Discussion

The calculated dihedral angles are nearly normally distributed with a peak around 70° (Figure 5). The majority of the identified conjugate faults are thus at higher angles compared to optimal orientations predicted based on the Mohr-Coulomb theory (Anderson, 1951; Sibson, 1974), and observed e.g. in areas of fluid-induced seismicity in the central US (e.g., Alt & Zoback, 2017; Schoenball & Ellsworth, 2017; Skoumal et al., 2019), but similar to those observed in the Ridgecrest area of the Eastern California Shear Zone (e.g., Ross et al., 2019; Fialko & Jin, 2021; Fialko, 2021). The characteristic dimensions of faults or active fault patches used in our analysis vary from 75 m to 3 km, with the mean value of 0.5 km (Figures S4–S16). Rupture dimensions of individual earthquakes comprising the respective earthquake clusters are smaller still. The small rupture size has several implications. First, a substantial fraction of the identified small-scale ruptures are not associated with mature well-slipped faults, and thus not linked to the ductile substrate, precluding a possibility that their orientations are controlled by localized shear zones below the brittle-ductile transition (e.g., Takeuchi & Fialko, 2012, 2013; Fialko & Jin, 2021; Scholz & Choi, 2022; Liang et al., 2021). Second, small ruptures are not expected to produce strong dynamic weakening, so that their strength may be to the first order governed by quasi-static friction (e.g., Lapusta & Rice, 2003; Fialko, 2015).

In the area of interest, the principal axes of both the maximum horizontal shortening rate (Figure S3) and maximum compressive stress (Yang & Hauksson, 2013) are oriented approximately north-south. Results shown in Figure 4 indicate that populations of right- and left-lateral faults are not symmetrically distributed around the axis of the maximum shortening rate and/or compression. While most of the right-lateral faults are at angles of 45±15 degrees to the principal strain rate/stress axis (Figure 4), most of the left-lateral faults are at more acute angles of 20-30°, nearly optimally oriented assuming the Byerlee's law (i.e., the coefficient of friction of 0.6-0.8). This is different from the observed fault orientations in Ridgecrest, where the dihedral angles between conjugate faults are approximately bisected by the principal strain rate and stress axes (Fialko & Jin, 2021; Fialko, 2021).

Assuming that the currently active left- and right-lateral faults initially formed at equal angles to the principal compression axis, and that their relative orientations with respect to each other have not changed over time, the data shown in Figure 4 might be interpreted as indicating a counter-clockwise rotation of the entire fault system by 10-15 degrees. One possible mechanism for such rotation is a preferred development and growth of right-lateral faults. It is known that slip on a fault embedded in an elastic medium results in fault rotation,

$$\omega = \arctan\left(\frac{1-2\nu}{2G}\Delta\tau\right), \tag{1}$$

where ω is the rotation angle in radians, G the shear modulus, ν the Poisson's ratio, and $\Delta\tau$ the stress drop (Martel, 1999). For an infinitely long strike-slip fault with a constant stress drop, the relation between the stress drop $\Delta\tau$ and surface fault slip s is:

$$\Delta\tau = \frac{1}{2}\frac{sG}{D}, \tag{2}$$

where D is the fault locking depth (e.g., Segall, 2010, p. 96). From equations 1 and 2, a strike-slip fault with a total offset s rotates by an angle

$$\omega = \arctan\left(\frac{1-2\nu}{4}\frac{s}{D}\right). \tag{3}$$

For right-lateral slip, the predicted sense of rotation is counter-clockwise (Martel, 1999). The estimated total offset on the San Jacinto Fault system that dominates interseismic deformation in the study area is 20-25 km (e.g., Morton & Matti, 1993). For $\nu = 0.25$ and $D = 12$ km (Lindsey et al., 2014; Tymofyeyeva & Fialko, 2018), equation 3 suggests a rotation of 12-15 degrees. Using a depth-averaged slip instead of surface slip in equation 3 reduces the estimated rotation by a few degrees. This is a lower bound on the total possible rotation amount because it neglects contributions from other major faults such as the Elsinore fault, as well as the distributed deformation due to numerous small faults in the bulk of the brittle upper crust (e.g., Fialko & Jin, 2021).

A common rotation away from the optimal orientation however suggests θ_0 of 35 degrees, and $\mu < 0.4$, lower than predicted by the Byerlee's law. Another possibility is that the relatively small and immature left-lateral faults are optimally oriented assuming Byerlee's friction. The same may be true for immature right-lateral faults, however the QLCs that are associated with major right-lateral faults (Figure 2) likely owe their orientations to the long-term fault rotation, as discussed above.

We interpret differences between the observed distributions of dihedral angles in different tectonic areas in terms of the amount of a total accommodated strain. In case of injection-induced seismicity in the central US (Alt & Zoback, 2017; Schoenball & Ellsworth, 2017; Skoumal et al., 2019), pre-existing faults are brought to failure due to increases in the pore fluid pressure, resulting in a preferential activation of faults that are optimally oriented with respect to the background stress. The Ridgecrest, eastern California, region is a developing shear zone, where new and pre-existing faults are continually activated and rotated primarily via distributed failure and simple shear (Fialko & Jin, 2021). The Anza-Borrego shear zone exemplifies a "high strain" end-member, whereby much of the deformation and rotation (Hauksson et al., 2022) is accommodated by well-developed plate boundary faults. The main difference between the observed orientations of small active faults in the Ridgecrest area of the Eastern California Shear Zone and the Anza-Borrego Shear Zone is that the latter features a non-symmetric distribution of conjugate faults with respect to the principal compression and shortening rate axes (Figure 4), likely due to different amounts of slip accommodated by the respective fault systems. At the initial stages of the shear zone development, synthetic (right-lateral) faults are rotated less than the antithetic (left-lateral) faults (Fialko & Jin, 2021) and are thus favored to grow. A continued slip on mature right-lateral faults rotates immature left-lateral faults toward the principal compression axis, which may eventually deactivate the rotated left-lateral faults and initiate slip on new or pre-existing left-lateral faults that are more optimally oriented for failure. Mature well-slipped faults may also develop deep crustal "roots" (Takeuchi & Fialko, 2012; Leloup et al., 1995; Jin et al., 2023) which can stabilize the fault orientation at $\sim$45 degrees to the principal shortening axis (i.e., optimal for ductile shear), potentially explaining the observed near-orthogonal orientations of mature conjugate faults (Thatcher & Hill, 1991; Yue et al., 2012; Fialko & Jin, 2021). Under this model, deep shear zones are the consequence, rather than the cause, of fault development in the brittle upper crust.

3 Conclusions

We used a new algorithm to quantify orientations of small active faults at the southern end of the San Andreas-San Jacinto fault system, referred to as the Anza-Borrego shear zone. The dihedral angles between conjugate strike-slip faults are nearly normally distributed with a mean value of $\sim 70°$. The fault strikes are asymmetrically distributed with respect to the principal strain rate and stress axes, with left-lateral faults optimally oriented for failure assuming the Byerlee's law, and right-lateral faults rotated by $\sim$10-20° counter-clockwise from the optimal orientation. We argue that the observed high-angle conjugate faults are not due to either low coefficient of friction or ductile shear zones in the lower crust, but can instead be explained by rotation due to a long-term tectonic deformation. Faults may form or be activated at near-optimal orientations, and subsequently rotate away from the principle shortening axis. A comparison to other areas of well-documented small active faults reveals an increase in the average dihedral angle with the total accumulated tectonic strain. We attribute the observed asymmetric distribution of conjugate faults with respect to the principal strain rate axis to a difference in the total amount of slip accommodated by the right- and left-lateral fault systems.

Acknowledgments

We thank the two anonymous reviewers for thoughtful comments that helped improve this manuscript. This study was supported by grants from NSF (EAR-1841273) and NASA (80NSSC22K0506) to YF. Figures were produced using Generic Mapping Tools (GMT) (Wessel et al., 2013) and Matlab. The authors declare no competing interests.

Data Availability Statement

LINSCAN source codes with examples and the QLC data used in our analysis are available at `https://doi.org/10.5281/zenodo.8356590`

References

Alt, R., & Zoback, M. (2017). In situ stress and active faulting in Oklahoma. *Bull. Seism. Soc. Am.*, *107*, 216–228.

Anderson, E. M. (1951). *The dynamics of faulting and dike formation with application to Britain.* Edinburgh: 206 pp., Oliver and Boyd.

Ankerst, M., Breunig, M. M., Kriegel, H.-P., & Sander, J. (1999). Optics: ordering points to identify the clustering structure. *SIGMOD record*, *28*(2), 49-60.

Artusi, R., Verderio, P., & Marubini, E. (2002). Bravais-Pearson and Spearman correlation coefficients: meaning, test of hypothesis and confidence interval. *The*

International journal of biological markers, *17*, 148–151.

Brown, K. M., & Fialko, Y. (2012). "Melt welt" mechanism of extreme weakening of gabbro at seismic slip rates. *Nature*, *488*, 638–641.

Burov, E. B. (2011). Rheology and strength of the lithosphere. *Marine and Petroleum Geology*, *28*, 1402–1443.

Byerlee, J. (1978). Friction of rock. *Pure Appl. Geophys.*, *116*, 615–626.

Cheng, Y., Hauksson, E., & Ben-Zion, Y. (2023). Refined earthquake focal mechanism catalog for Southern California derived with deep learning algorithms. *J. Geophys. Res.*, *128*, e2022JB025975.

Cloos, E. (1955). Experimental analysis of fracture patterns. *Bull. Seism. Soc. Am.*, *66*, 241-256.

Coblentz, D. D., Richardson, R. M., & Sandiford, M. (1994). On the gravitational potential of the Earth's lithosphere. *Tectonics*, *13*, 929–945.

Cochran, E. S., Wickham-Piotrowski, A., Kemna, K. B., Harrington, R. M., Dougherty, S. L., & Castro, A. F. P. (2020). Minimal clustering of injection-induced earthquakes observed with a large-n seismic array. *Bull. Seism. Soc. Am.*, *110*, 2005–2017.

Crowell, B. W., Bock, Y., Sandwell, D. T., & Fialko, Y. (2013). Geodetic investigation into the deformation of the Salton Trough. *J. Geophys. Res.*, *118*, 5030–5039.

Di Toro, G., Han, R., Hirose, T., De Paola, N., Nielsen, S., Mizoguchi, K., … Shimamoto, T. (2011). Fault lubrication during earthquakes. *Nature*, *471*, 494–498.

Fialko, Y. (2015). Fracture and Frictional Mechanics - Theory. In G. Schubert (Ed.), *Treatise on geophysics, 2nd. ed., vol. 4* (pp. 73–91). Elsevier Ltd., Oxford.

Fialko, Y. (2021). Estimation of absolute stress in the hypocentral region of the 2019 Ridgecrest, California, earthquakes. *J. Geophys. Res.*, *126*, e2021JB022000.

Fialko, Y., & Jin, Z. (2021). Simple shear origin of the cross-faults ruptured in the 2019 Ridgecrest earthquake sequence. *Nature Geoscience*, *14*, 513–518.

Fialko, Y., Rivera, L., & Kanamori, H. (2005). Estimate of differential stress in the upper crust from variations in topography and strike along the San Andreas fault. *Geophys. J. Int.*, *160*, 527–532.

Freund, R. (1970). Rotation of strike slip faults in Sistan, southeast Iran. *The Jour-*

nal of Geology, *78*, 188–200.

Gonzalez-Ortega, A., Fialko, Y., Sandwell, D., Alejandro Nava-Pichardo, F., Fletcher, J., Gonzalez-Garcia, J., . . . Funning, G. (2014). El Mayor-Cucapah (M_w7.2) earthquake: Early near-field postseismic deformation from InSAR and GPS observations. *J. Geophys. Res.*, *119*, 1482–1497.

Hatch-Ibarra, R. L., Abercrombie, R. E., Ruhl, C. J., Smith, K. D., Hammond, W. C., & Pierce, I. K. (2022). The 2016 Nine Mile Ranch Earthquakes: Hazard and Tectonic Implications of Orthogonal Conjugate Faulting in the Walker Lane. *Bull. Seism. Soc. Am.*, *112*, 1727-1741.

Hauksson, E., Stock, J. M., & Husker, A. L. (2022). Seismicity in a weak crust: the transtensional tectonics of the Brawley Seismic Zone section of the Pacific–North America Plate Boundary in Southern California, USA. *Geophys. J. Int.*, *231*, 717-735.

Herzig, C. T., & Jacobs, D. C. (1994). Cenozoic volcanism and two-stage extension in the Salton trough, southern California and northern Baja California. *Geology*, *22*, 991–994.

Jennings, C., & Bryant, W. (2010). *Fault Activity Map of California.* (California Division of Mines and Geology, Geologic Data Map No. 6)

Jin, Z., & Fialko, Y. (2020). Finite slip models of the 2019 Ridgecrest earthquake sequence constrained by space geodetic data and aftershock locations. *Bull. Seism. Soc. Am.*, *110*, 1660–1679.

Jin, Z., Fialko, Y., Yang, H., & Li, Y. (2023). Transient deformation excited by the 2021 M7.4 Maduo (China) earthquake: Evidence of a deep shear zone. *J. Geophys. Res.*, *128*, e2023JB026643.

Lapusta, N., & Rice, J. (2003). Nucleation and early seismic propagation of small and large events in a crustal earthquake model. *J. Geophys. Res.*, *108*.

Leloup, P. H., Lacassin, R., Tapponnier, P., Schärer, U., Zhong, D., Liu, X., . . . Trinh, P. T. (1995). The Ailao Shan-Red River shear zone (Yunnan, China), Tertiary transform boundary of Indochina. *Tectonophysics*, *251*(1), 3–84.

Liang, C., Ampuero, J.-P., & Pino Muñoz, D. (2021). Deep ductile shear zone facilitates near-orthogonal strike-slip faulting in a thin brittle lithosphere. *Geophys. Res. Lett.*, *48*, e2020GL090744.

Lindsey, E. O., Sahakian, V. J., Fialko, Y., Bock, Y., Barbot, S., & Rockwell, T. K.

(2014). Interseismic strain localization in the San Jacinto fault zone. *Pure and Applied Geophysics*, *171*(11), 2937–2954.

Martel, S. J. (1999). Mechanical controls on fault geometry. *J. Struct. Geol.*, *21*, 585–596.

McGill, S. F., Allen, C. R., Hudnut, K. W., Johnson, D. C., Miller, W. F., & Sieh, K. E. (1989). Slip on the Superstition Hills fault and on nearby faults associated with the 24 November 1987 Elmore Ranch and Superstition Hills earthquakes, southern California. *Bull. Seism. Soc. Am.*, *79*, 362–375.

Middleton, T. A., & Copley, A. (2014). Constraining fault friction by re-examining earthquake nodal plane dips. *Geophys. J. Int.*, *196*, 671–680.

Morton, D., & Matti, J. (1993). Extension and contraction within an evolving divergent strike slip fault complex: The San Andreas and San Jacinto fault zones at their convergence in Southern California. In R. J. W. R. E. Powell & J. C. Matti (Eds.), *The san andreas fault system: Displacement, palinspastic reconstruction, and geologic evolution* (pp. 217–230). Geological Society of America Memoir.

Mount, V., & Suppe, J. (1987). State of stress near the San Andreas fault: Implications for wrench tectonics. *Geology*, *15*, 1143–1146.

Nadeau, R. M., & McEvilly, T. V. (1999). Fault slip rates at depth from recurrence intervals of repeating microearthquakes. *Science*, *285*, 718–721.

Nur, A., Ron, H., & Scotti, O. (1986). Fault mechanics and the kinematics of block rotations. *Geology*, *14*, 746–749.

Rice, J. R. (2006). Heating and weakening of faults during earthquake slip. *J. Geophys. Res.*, *111*, B05311.

Ross, Z. E., Idini, B., Jia, Z., Stephenson, O. L., Zhong, M., Wang, X., … others (2019). Hierarchical interlocked orthogonal faulting in the 2019 Ridgecrest earthquake sequence. *Science*, *366*, 346–351.

Schoenball, M., & Ellsworth, W. L. (2017). A systematic assessment of the spatiotemporal evolution of fault activation through induced seismicity in Oklahoma and southern Kansas. *J. Geophys. Res.*, *122*, 10–189.

Scholz, C. H. (2019). *The mechanics of earthquakes and faulting.* New York, NY: 3rd Ed., 493 pp., Cambidge Univ. Press.

Scholz, C. H., & Choi, E. (2022). What comes first: The fault or the ductile shear zone? *Earth Planet. Sci. Lett.*, *577*, 117273.

Schubert, E., Sander, J., Ester, M., Kriegel, H. P., & Xu, X. (2017). DBSCAN revisited, revisited: why and how you should (still) use DBSCAN. *ACM Transactions on Database Systems (TODS)*, *42*, 1–21.

Segall, P. (2010). *Earthquake and volcano deformation.* Princeton University Press.

Sibson, R. H. (1974). Frictional constraints on thrust, wrench and normal faults. *Nature*, *249*, 542–544.

Sibson, R. H. (1990). Rupture nucleation on unfavorably oriented faults. *Bull. Seism. Soc. Am.*, *80*, 1580–1604.

Sibson, R. H. (1994). An assessment of field evidence for byerlee friction. *Pure Appl. Geophys.*, *142*, 645–662.

Skoumal, R. J., Kaven, J. O., & Walter, J. I. (2019). Characterizing seismogenic fault structures in Oklahoma using a relocated template-matched catalog. *Seismol. Res. Lett.*, *90*, 1535–1543.

Takeuchi, C., & Fialko, Y. (2012). Dynamic models of interseismic deformation and stress transfer from plate motion to continental transform faults. *J. Geophys. Res.*, *117*, B05403.

Takeuchi, C., & Fialko, Y. (2013). On the effects of thermally weakened ductile shear zones on postseismic deformation. *J. Geophys. Res.*, *118*, 6295–6310.

Thatcher, W., & Hill, D. P. (1991). Fault orientations in extensional and conjugate strike-slip environments and their implications. *Geology*, *19*, 1116-1120.

Townend, J., & Zoback, M. (2000). How faulting keeps the crust strong. *Geology*, *28*, 399–402.

Twiss, R., & Moores, E. (1992). *Structural geology.* New York, NY: W.H. Freeman.

Tymofyeyeva, E., & Fialko, Y. (2018). Geodetic evidence for a blind fault segment at the Southern end of the San Jacinto Fault Zone. *J. Geophys. Res.*, *123*, 878–891.

Valoroso, L., Improta, L., Chiaraluce, L., Di Stefano, R., Ferranti, L., Govoni, A., & Chiarabba, C. (2009). Active faults and induced seismicity in the Val d'Agri area (Southern Apennines, Italy). *Geophys. J. Int.*, *178*, 488–502.

Walsh, J., & Watterson, J. (1988). Dips of normal faults in British Coal Measures and other sedimentary sequences. *Journal of the Geological Society*, *145*, 859–873.

Wernicke, B. (1995). Low-angle normal faults and seismicity: A review. *J. Geophys. Res.*, *100*, 20159–20174.

Wessel, P., Smith, W. H. F., Scharroo, R., Luis, J., & Wobbe, F. (2013). Generic Mapping Tools: Improved Version Released. *Eos, Trans. AGU*, *94*, 409–410.

Yang, W., & Hauksson, E. (2013). The tectonic crustal stress field and style of faulting along the Pacific North America Plate boundary in Southern California. *Geophys. J. Int.*, *194*, 100–117.

Yue, H., Lay, T., & Koper, K. D. (2012). En échelon and orthogonal fault ruptures of the 11 april 2012 great intraplate earthquakes. *Nature*, *490*, 245–249.

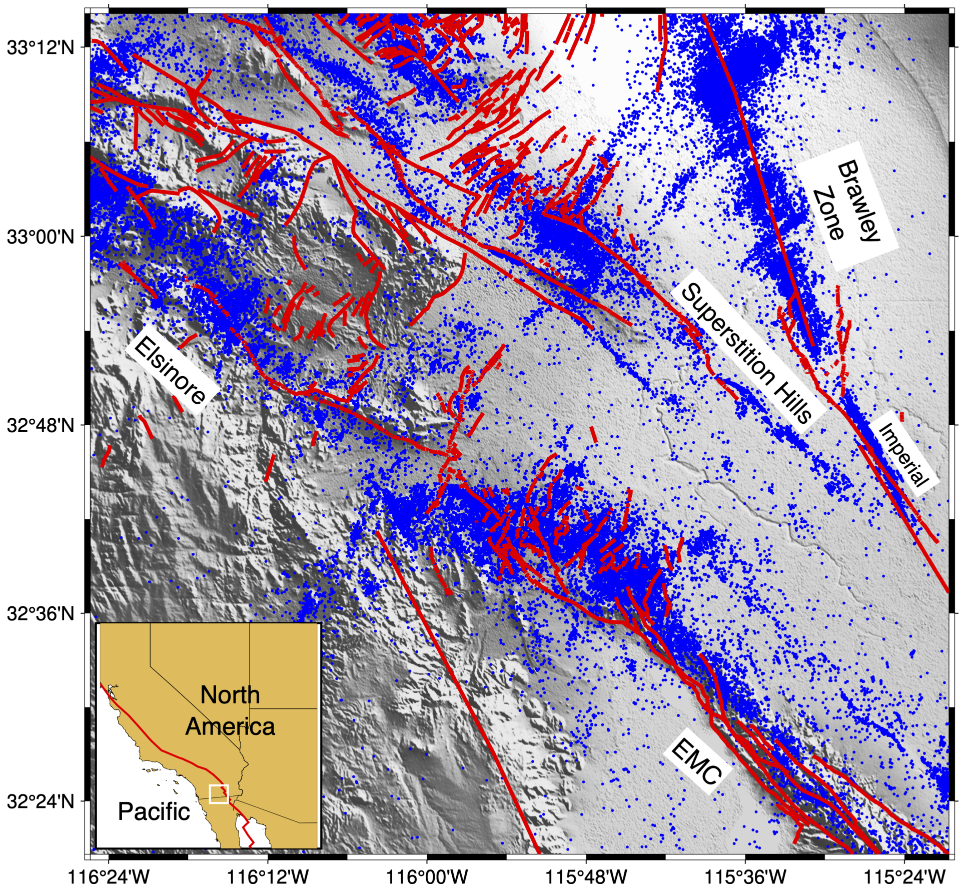

Figure 1. Map of the study area, with shaded relief. Red lines denote traces of Quaternary faults (Jennings & Bryant, 2010). Blue dots denote earthquake epicenters from Cheng et al. (2023) catalog. EMC="El Mayor-Cucapah". The inset shows the regional setting with respect to the North America-Pacific plate boundary (red line).

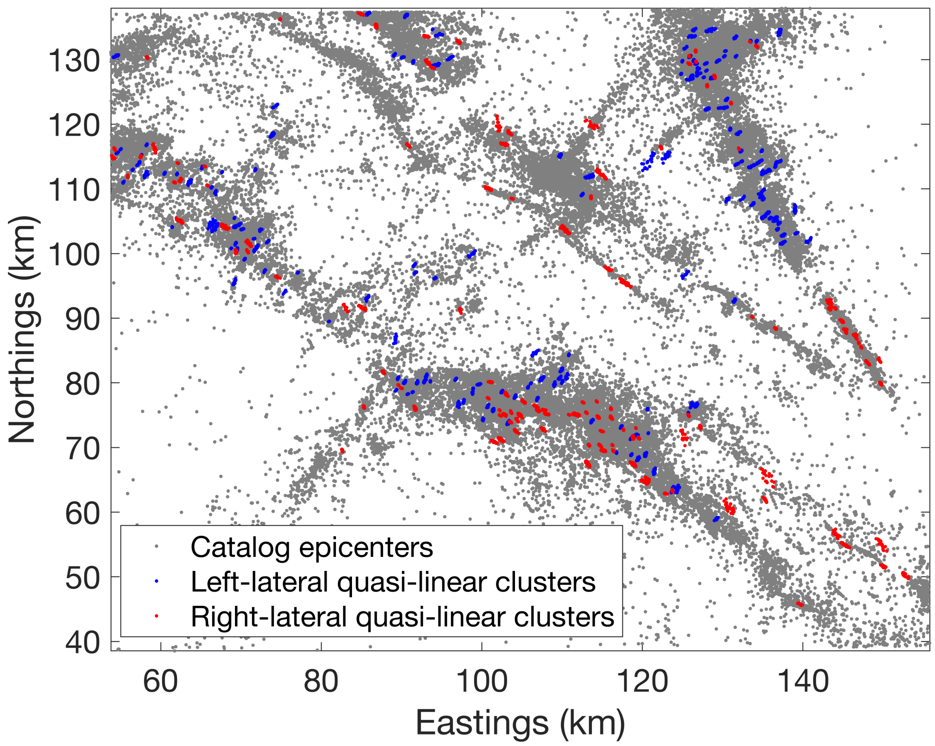

Figure 2. Grey dots: catalog epicenters (same as in Figure 1). Red and blue dots: quasi-linear clusters of epicenters with right- and left-lateral sense of slip, respectively, identified by our analysis. A total of 332 clusters are shown, including 195 left-lateral clusters and 137 right-lateral clusters. The minimum and maximum cluster lengths are 76 m and 3.05 km, respectively.

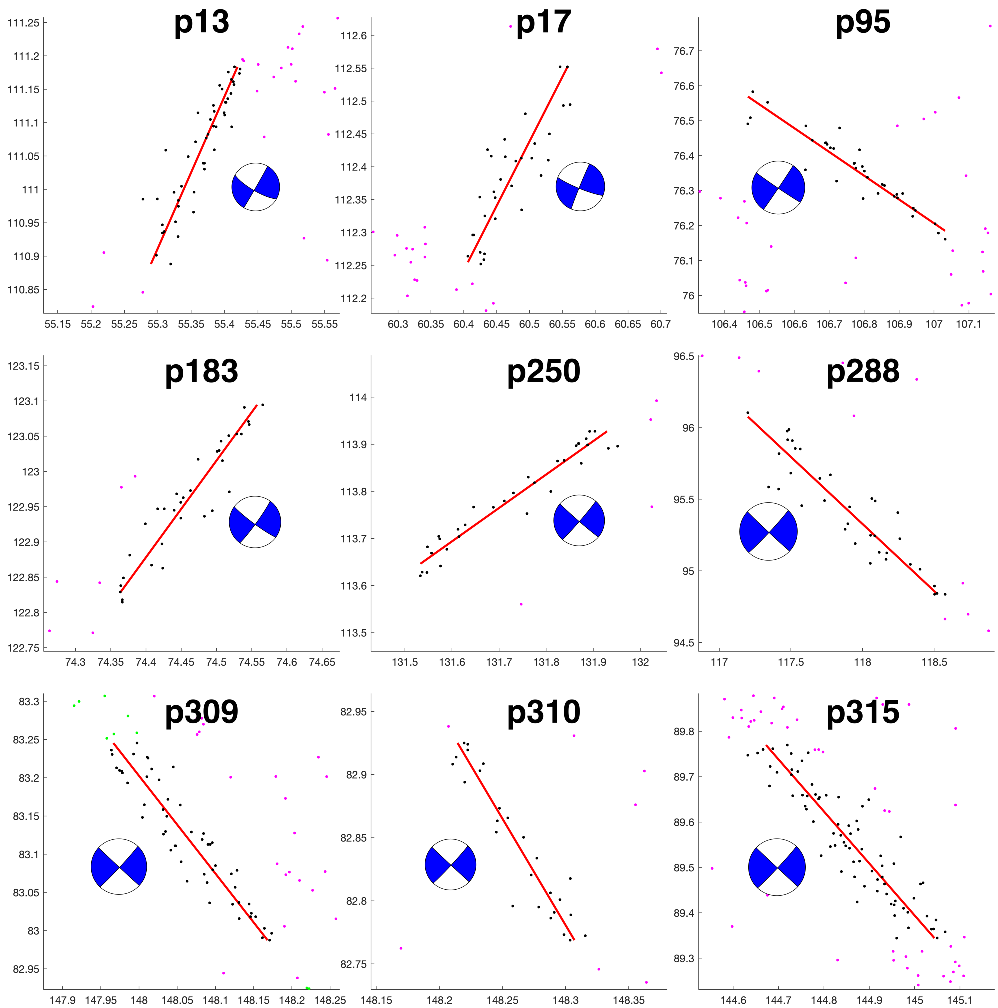

Figure 3. Examples of quasi-linear clusters (QLCs) that passed the quality control checks. Black dots denote earthquakes constituting a cluster, and magenta dots denote the background seismicity. Red lines denote best-fitting linear segments. Blue beach balls denote composite focal mechanisms. Numerical labels denote cluster numbers (see Supplementary Figures S5-S16). Axes represent northing and easting coordinates, in km.

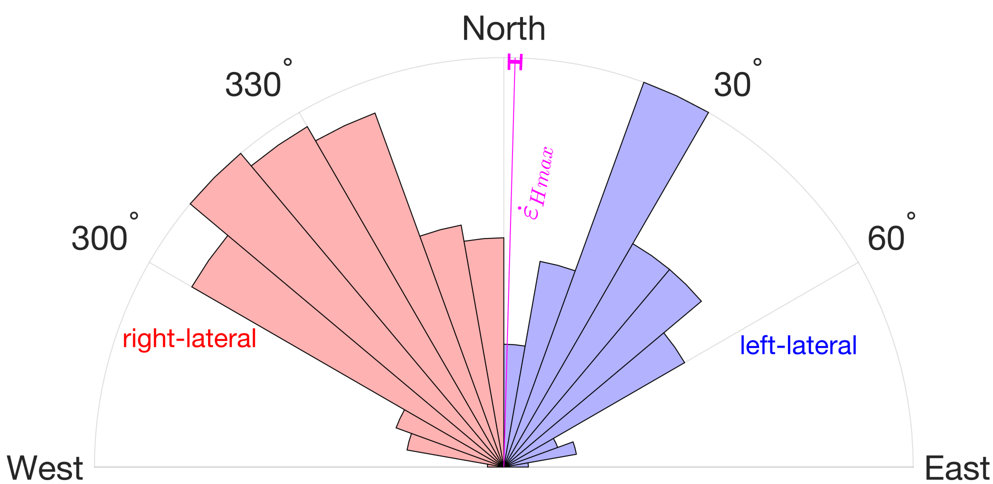

Figure 4. A distribution of strike angles of high-quality QLCs shown in Figures 3 and S4-S16. Red histogram corresponds to right-lateral faults (total of 137 samples), and blue histogram corresponds to left-lateral faults (total of 195 samples). Thin magenta line denotes the average orientation of the principal shortening rate axis (see Figure S3). The magenta error bar denotes 4 standard deviations.

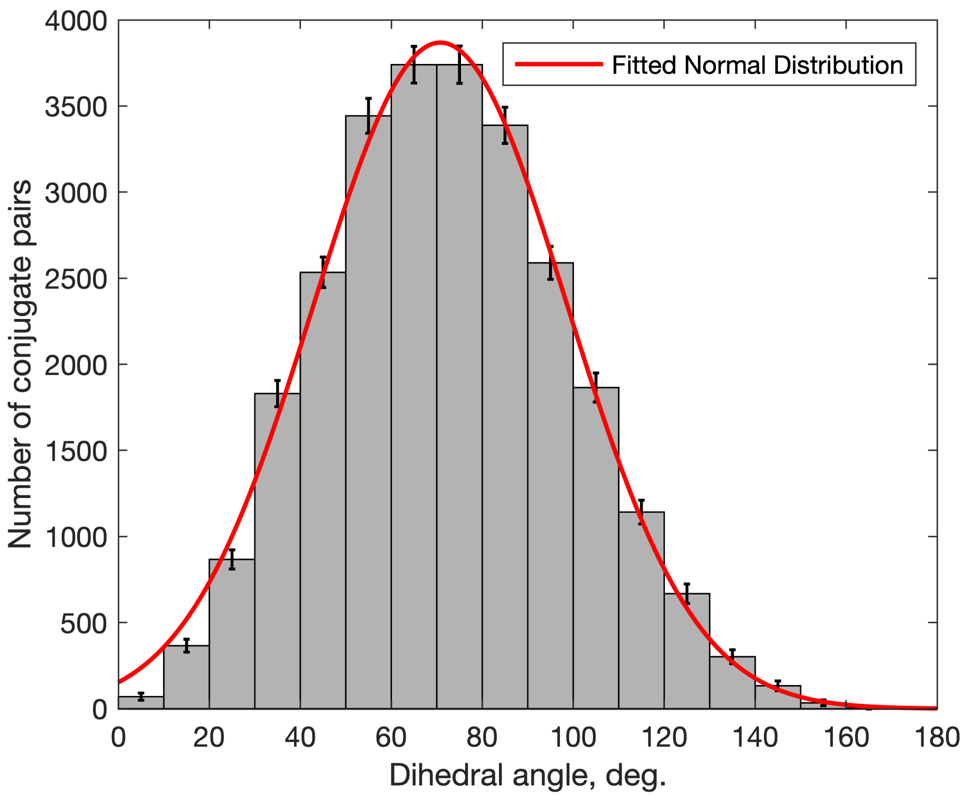

Figure 5. A histogram of dihedral angles between the conjugate strike-slip faults shown in Figure 4. Dihedral angles were computed between every possible pair of right- and left-lateral faults. Error bars denote 2σ uncertainty (see Fialko (2021) for details of the error analysis). The red curve denotes the best-fitting Gaussian distribution. The mean is 70.8 and the standard deviation is 28.9 degrees.

Supporting Information for "High-angle orientations of active conjugate faults in the Anza-Borrego shear zone, Southern California"

Xiaoyu Zou[1], Yuri Fialko[1], Andrew Dennehy[2], Alexander Cloninger[3,4],

Shabnam J. Semnani[5]

[1]Institute of Geophysics and Planetary Physics, Scripps Institution of Oceanography, University of California San Diego, La Jolla, CA 92093, USA.

[2]Committe on Computational and Applied Mathematics, University of Chicago, Chicago, IL 60615, USA.

[3]Department of Mathematical Sciences, University of California San Diego, La Jolla, CA 92093, USA.

[4]Halıcıoğlu Data Science Institute, University of California San Diego, La Jolla, CA 92093, USA

[5]Department of Structural Engineering, University of California San Diego, La Jolla, CA 92093, USA.

Contents of this file

Corresponding author: Xiaoyu Zou, Institute of Geophysics and Planetary Physics, University of California, San Diego, 8800 Biological Grade, La Jolla, CA, 92093. (x3zou@ucsd.edu)

Text S1. Description of LINSCAN algorithm

LINSCAN is based on OPTICS (Ordering Points to Identify the Clustering Structure), a density-based clustering algorithm. OPTICS uses three parameters for clustering, ϵ, $MinPts$, and ξ. ϵ is the maximum distance to consider when confining a cluster, $MinPts$ describes the minimum number of points required to define a cluster, and ξ determines the minimum steepness to determine the local minimum of *reachability distance*, which constitutes the boundary of a cluster. OPTICS first searches for *core points* in the data, which is defined as a point with at least $MinPts$ of points found within its neighborhood of ϵ distance. For each of the *core point*, it defines a *core distance*, which is the distance between a *core point* and its $MinPts$-th closest point. Next, OPTICS calculates the *reachability distance* among all core points. The *reachability distance* between points a and b is either the distance between a and b or the *core distance* of a, whichever is larger. Points that don't have at least $MinPts$ of points found within its neighborhood of ϵ distance won't be classified as a *core point*, so their *core distance* and *reachability distance* are undefined. Points within a cluster have a low *reachability distance* to their most adjacent neighbors, so points with local minimum *reachability distance* are identified as one cluster.

Since OPTICS uses the Euclidean metric to define clusters, the shape of clusters only depends on their density structure and is not necessarily linear. LINSCAN keeps the basic method of OPTICS but replaces the Euclidean metric with a distance function derived from Kullback-Leibler Divergence, which is the measurement of similarity between two distributions. In this way, the clustering results will be more linear. In LINSCAN we not only keep ϵ, $MinPts$, and ξ, but also introduce two additional parameters: *ecc_pts* and *threshold*. For each point, LINSCAN approximates its *ecc_pts* nearest neighbors as a normal distribution. Then, for clustering, we define the pairwise distance between $P = \mathcal{N}(\mu_P, \Sigma_P)$ and $Q = \mathcal{N}(\mu_Q, \Sigma_Q)$ to be:

$$\begin{aligned} D(P,Q) = \frac{1}{2}||\Sigma_Q^{-\frac{1}{2}}\Sigma_P\Sigma_Q^{-\frac{1}{2}} - I||_F \\ +\frac{1}{2}||\Sigma_P^{-\frac{1}{2}}\Sigma_Q\Sigma_P^{-\frac{1}{2}} - I||_F \\ +\frac{1}{\sqrt{2}}||\mu_P - \mu_Q||_{\Sigma_Q^{-1}} \\ +\frac{1}{\sqrt{2}}||\mu_P - \mu_Q||_{\Sigma_P^{-1}} \end{aligned} \tag{1}$$

where $||A||_F$ denotes the frobenius norm of the matrix A and

$$||x||_A = \sqrt{x^T A x} \tag{2}$$

denotes the elliptic norm defined by A for vector x and matrix A. This distance can be viewed as a low-order approximation of the symmetrized KL-divergence.

The *threshold* parameter represents the minimum correlation coefficient. All clusters with correlation coefficients lower than the *threshold* won't be included in the final result.

With all parameters being set, LINSCAN will go through each point in the dataset and label it either as a member of linear clusters with a sufficient correlation coefficient or an unqualified data point.

With synthetic data, LINSCAN is proven accurate in linear clustering. After testing LINSCAN on randomly generated synthetic data with noise, non-linear clusters, and linear clusters, we found that LINSCAN can correctly identify as many as 80% true linear cluster data points (Figure S1).

References

Fialko, Y., & Jin, Z. (2021). Simple shear origin of the cross-faults ruptured in the 2019 Ridgecrest earthquake sequence. *Nature Geoscience*, *14*, 513–518.

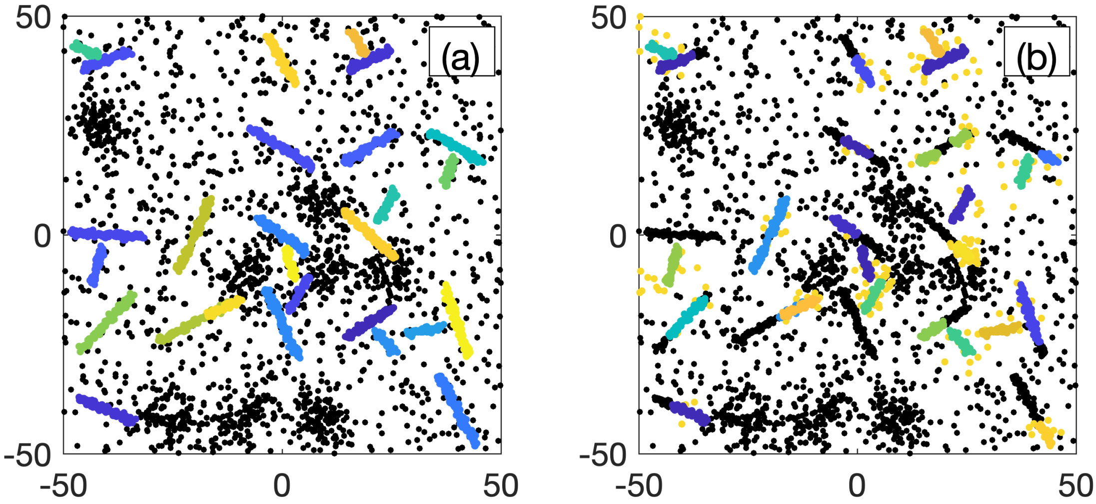

Figure S1. (a) A synthetic data set mimicking a distribution of earthquake epicenters. Black points represent "noise" (i.e., background seismicity, and irregular or quasi-isometric clusters). Linear clusters are denoted by sets of points having the same color (other than black). (b) LINSCAN classification: color (non-black) sets of points denote identified linear clusters, and black points represent the remaining data (i.e., data points that were not identified as belonging to a linear cluster).

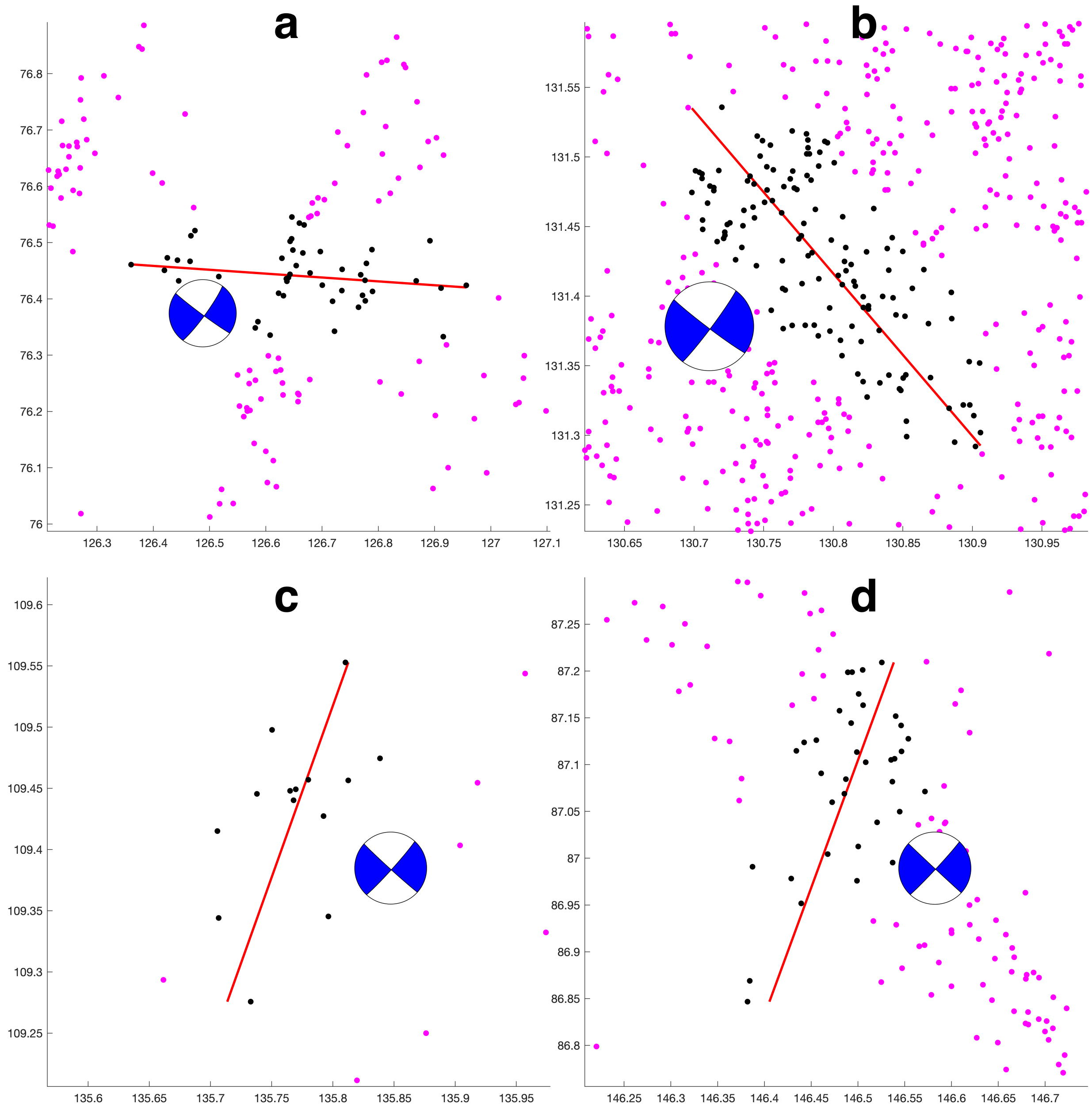

Figure S2. Examples of clusters selected by LINSCAN that failed to pass a visual quality check. Panels (a) and (d) illustrate clusters which contain smaller linear features that are not aligned with the overall trend. Panel (b) illustrates a selected cluster which is not obviously distinguishable from the background. Panel (c) illustrates a quasi-linear cluster with points that are unevenly and/or sparsely distributed.

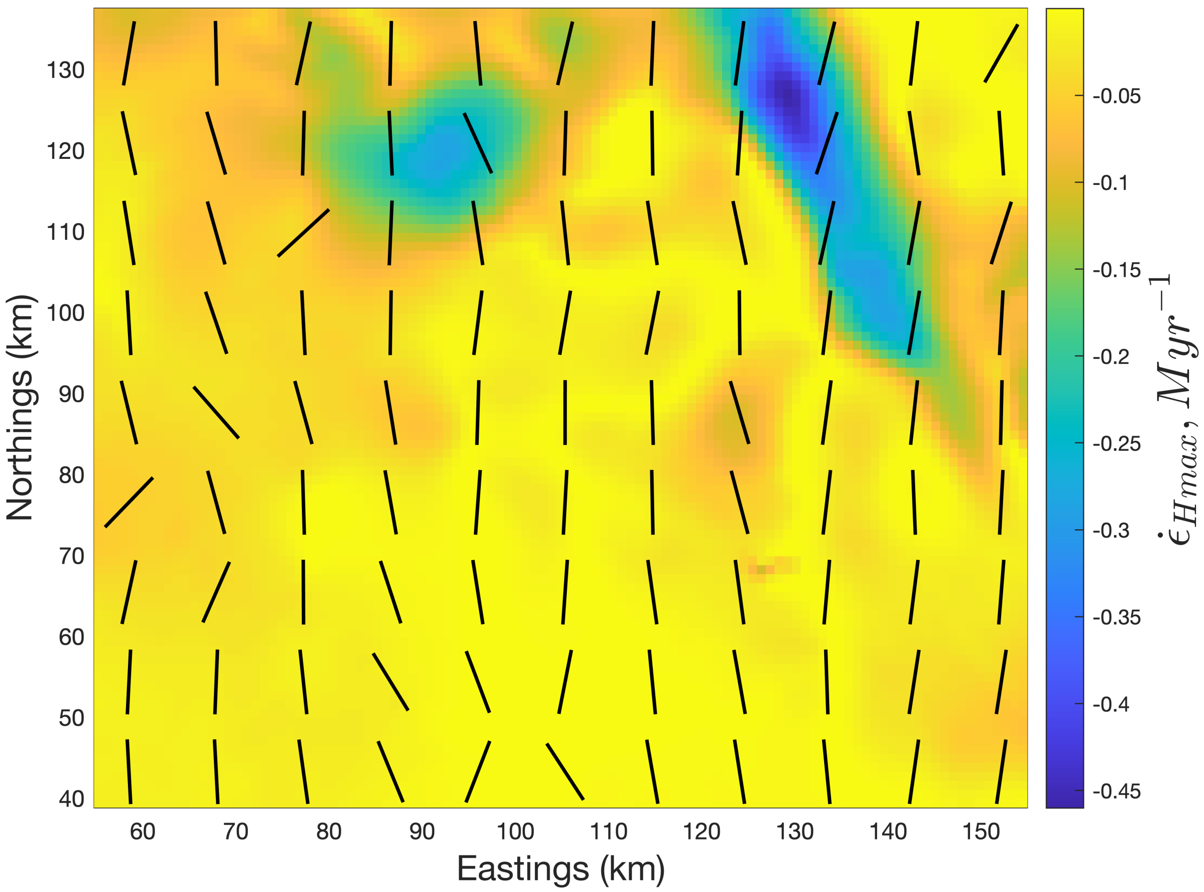

Figure S3. The magnitude (color) and orientation (black tick marks) of the maximum compressive strain rate in the study area calculated from the GNSS-derived secular velocities (for details, see Methods in Fialko & Jin, 2021).

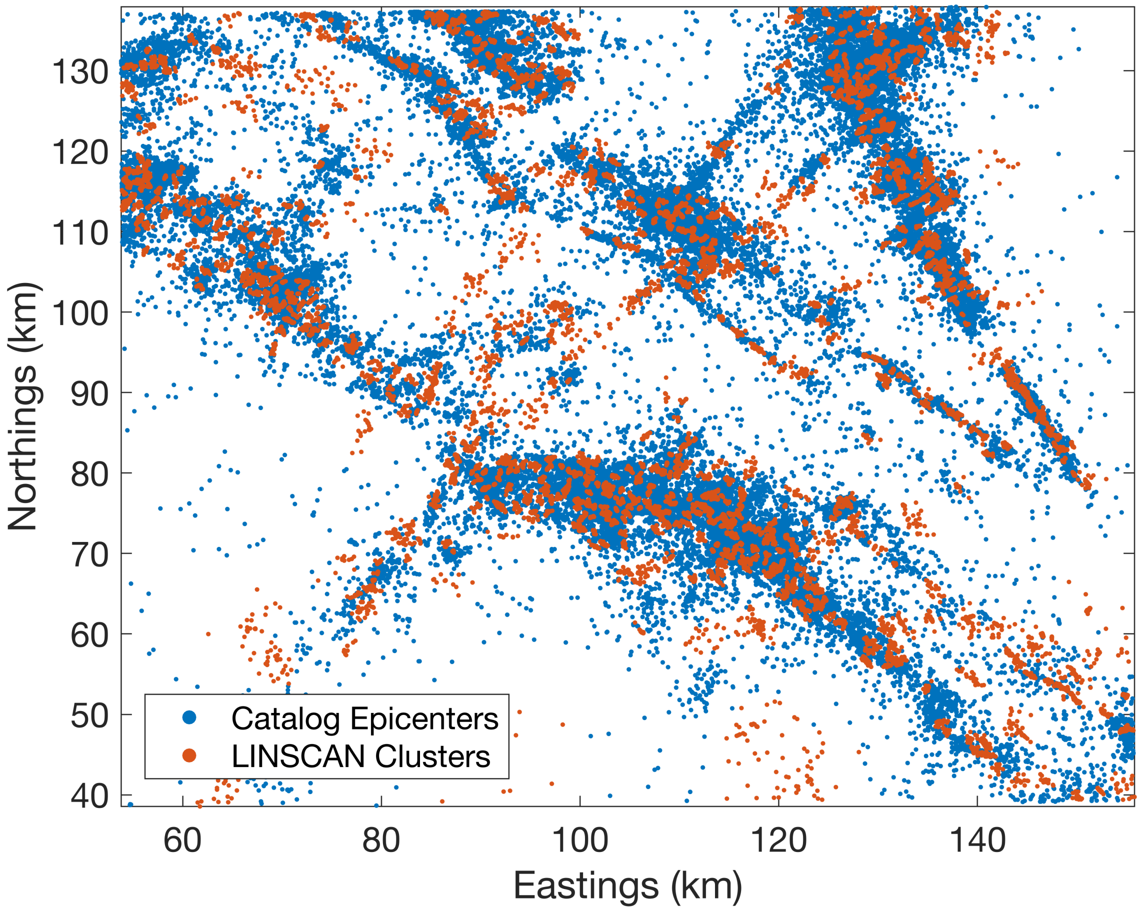

Figure S4. Catalog seismicity (blue dots, same as in Figure 1), and quasi-linear clusters (QLCs) of seismicity identified by the LINSCAN algorithm (orange dots). The total number of QLCs identified by LINSCAN is 1181.

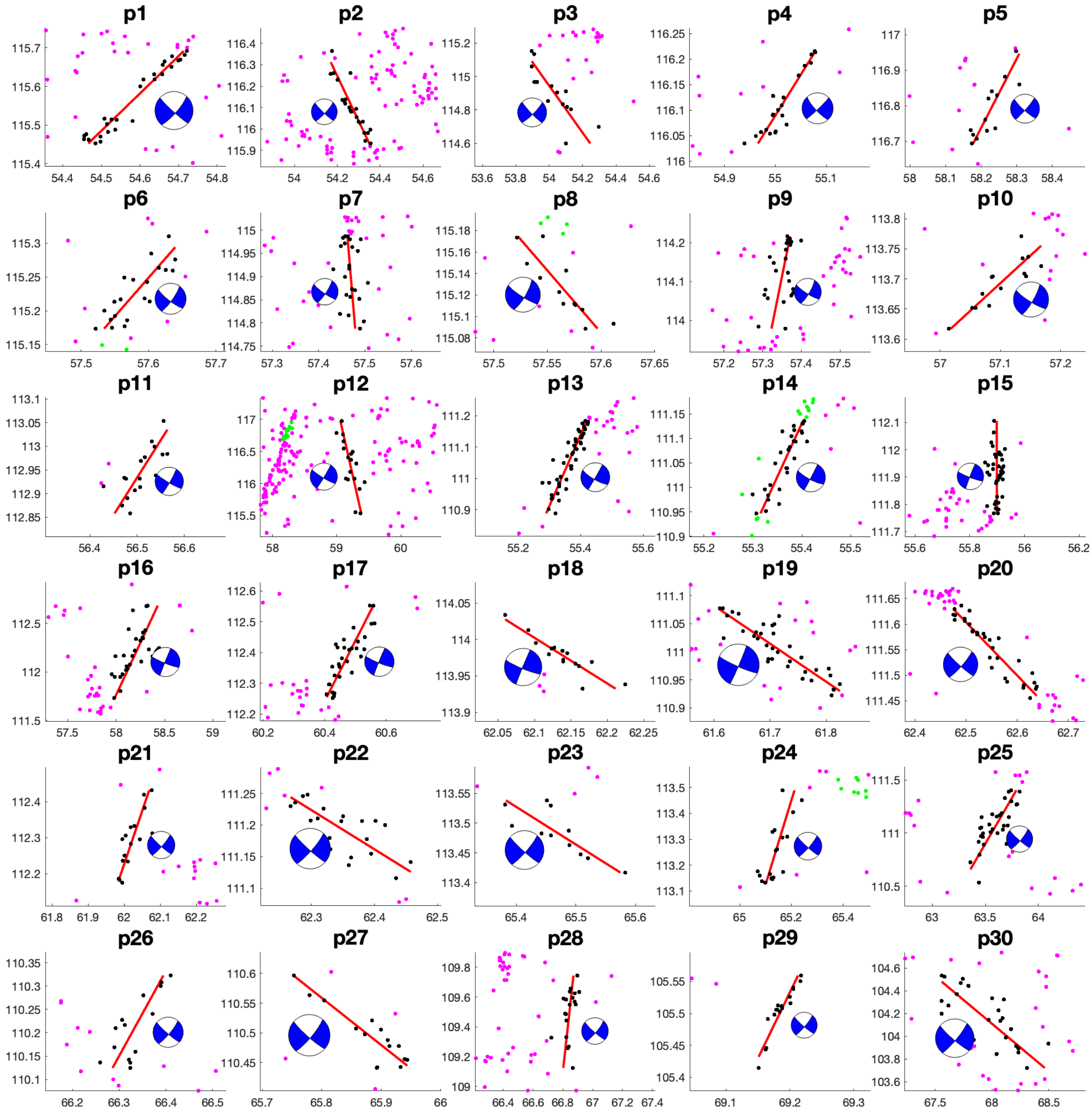

Figure S5. Close-up views of selected quasi-linear clusters. Each panel shows a quasi-linear cluster (black dots), along with a composite focal mechanism (blue beach ball). Solid red line denotes a best-fit line segment. Magenta dots denote background seismicity. Green dots denote other selected quasi-linear clusters.

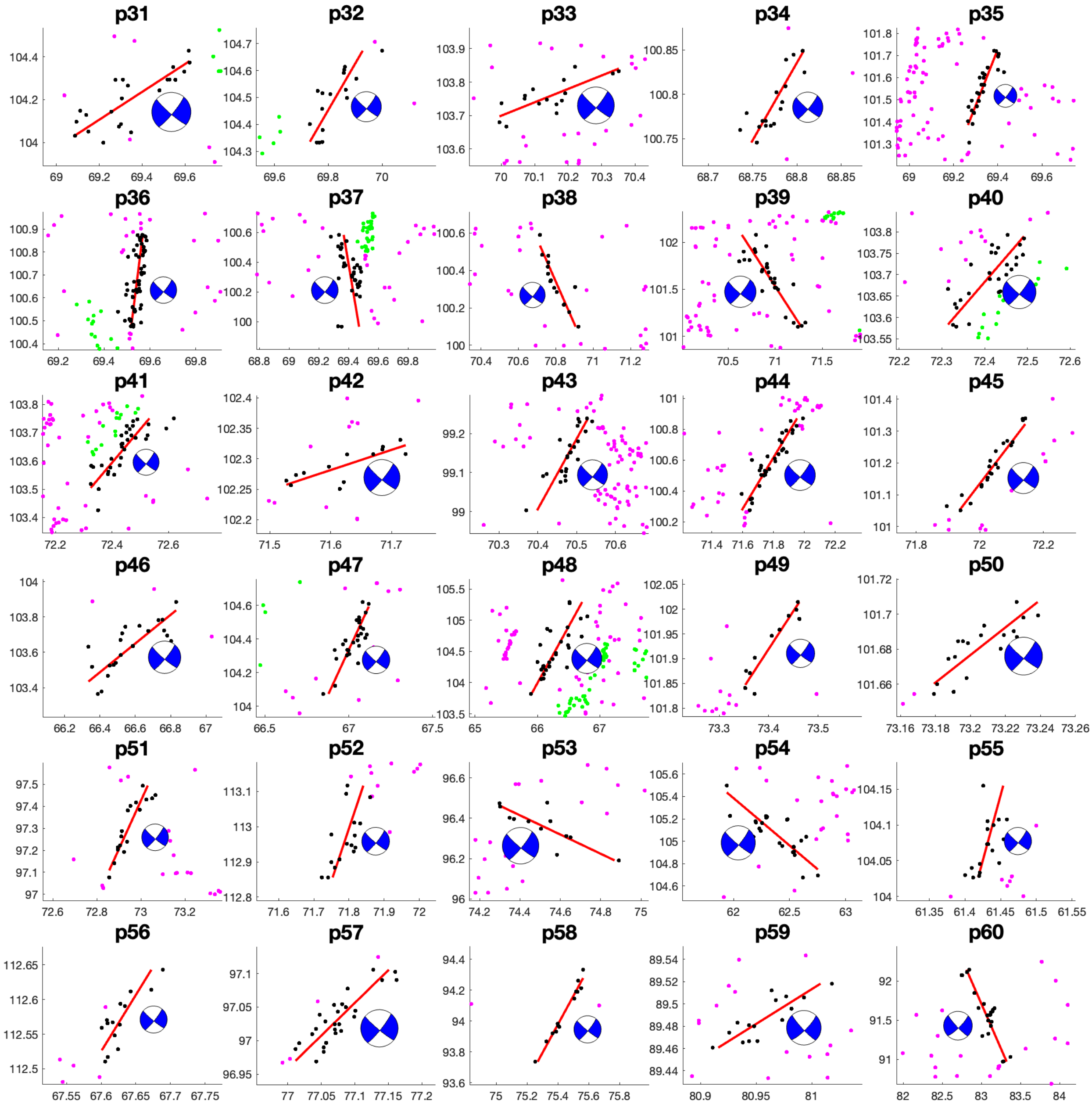

Figure S6. Close-up views of selected quasi-linear clusters. Each panel shows a quasi-linear cluster (black dots), along with a composite focal mechanism (blue beach ball). Solid red line denotes a best-fit line segment. Magenta dots denote background seismicity. Green dots denote other selected quasi-linear clusters.

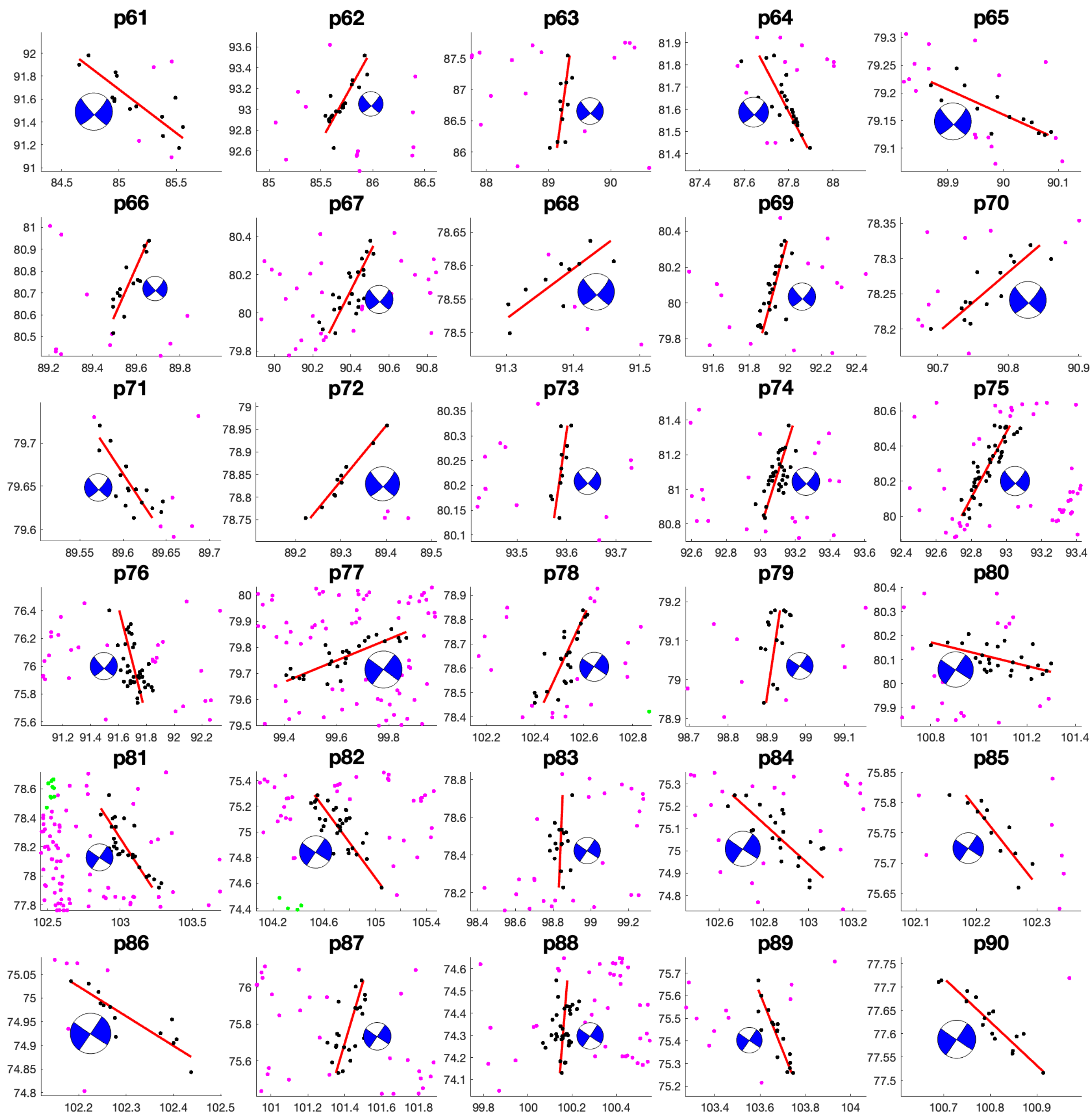

Figure S7. Close-up views of selected quasi-linear clusters. Each panel shows a quasi-linear cluster (black dots), along with a composite focal mechanism (blue beach ball). Solid red line denotes a best-fit line segment. Magenta dots denote background seismicity. Green dots denote other selected quasi-linear clusters.

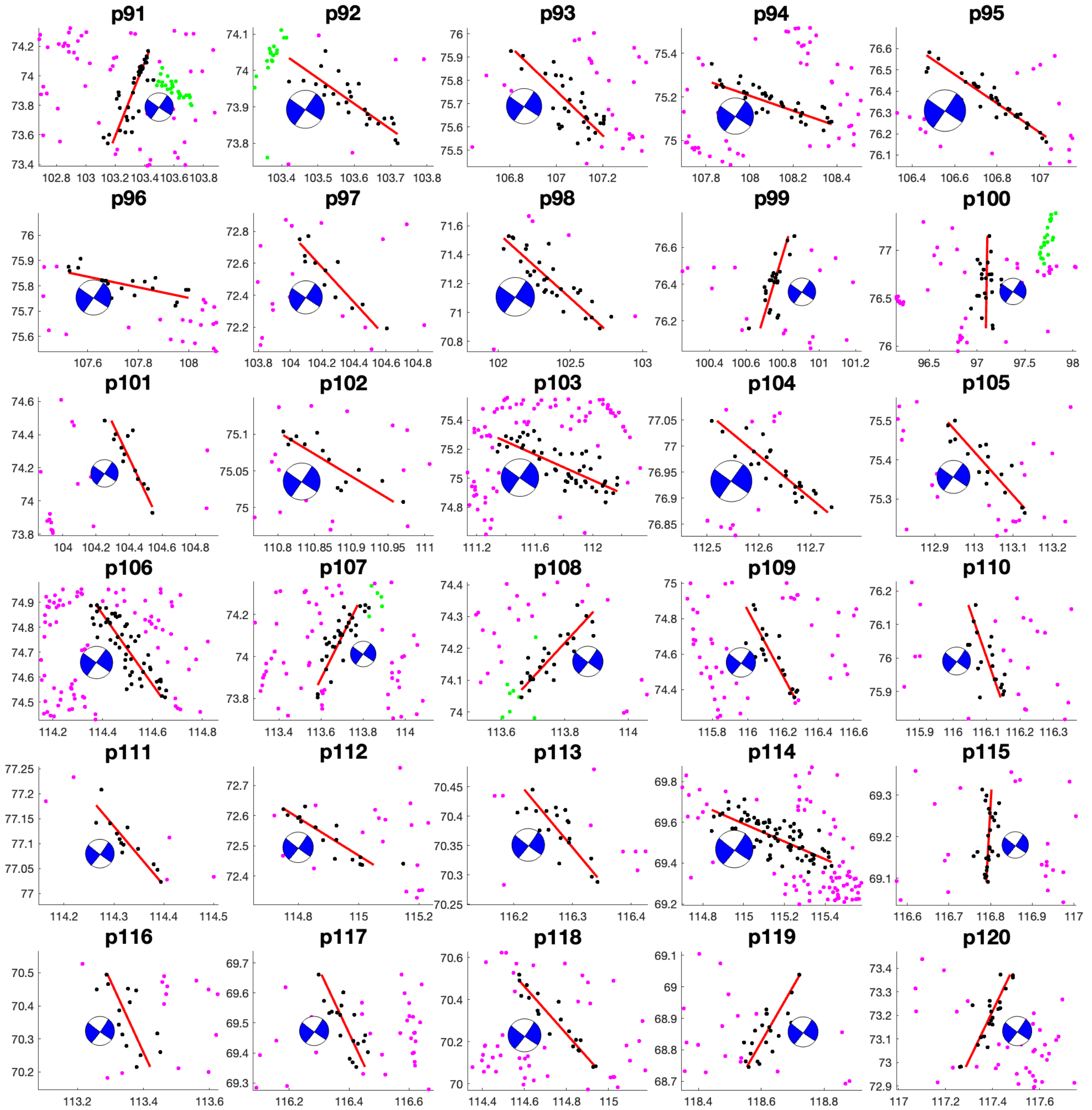

Figure S8. Close-up views of selected quasi-linear clusters. Each panel shows a quasi-linear cluster (black dots), along with a composite focal mechanism (blue beach ball). Solid red line denotes a best-fit line segment. Magenta dots denote background seismicity. Green dots denote other selected quasi-linear clusters.

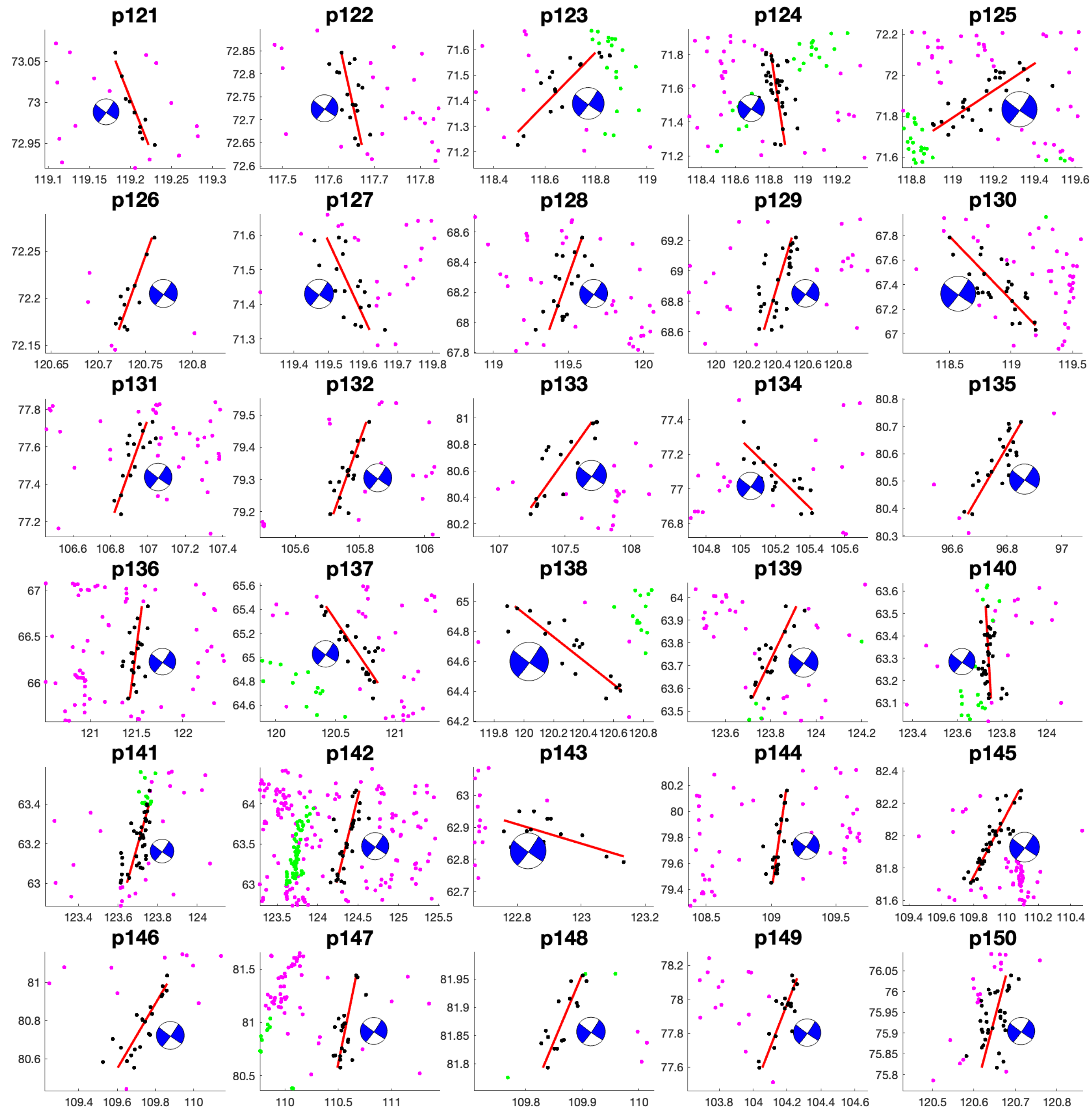

Figure S9. Close-up views of selected quasi-linear clusters. Each panel shows a quasi-linear cluster (black dots), along with a composite focal mechanism (blue beach ball). Solid red line denotes a best-fit line segment. Magenta dots denote background seismicity. Green dots denote other selected quasi-linear clusters.

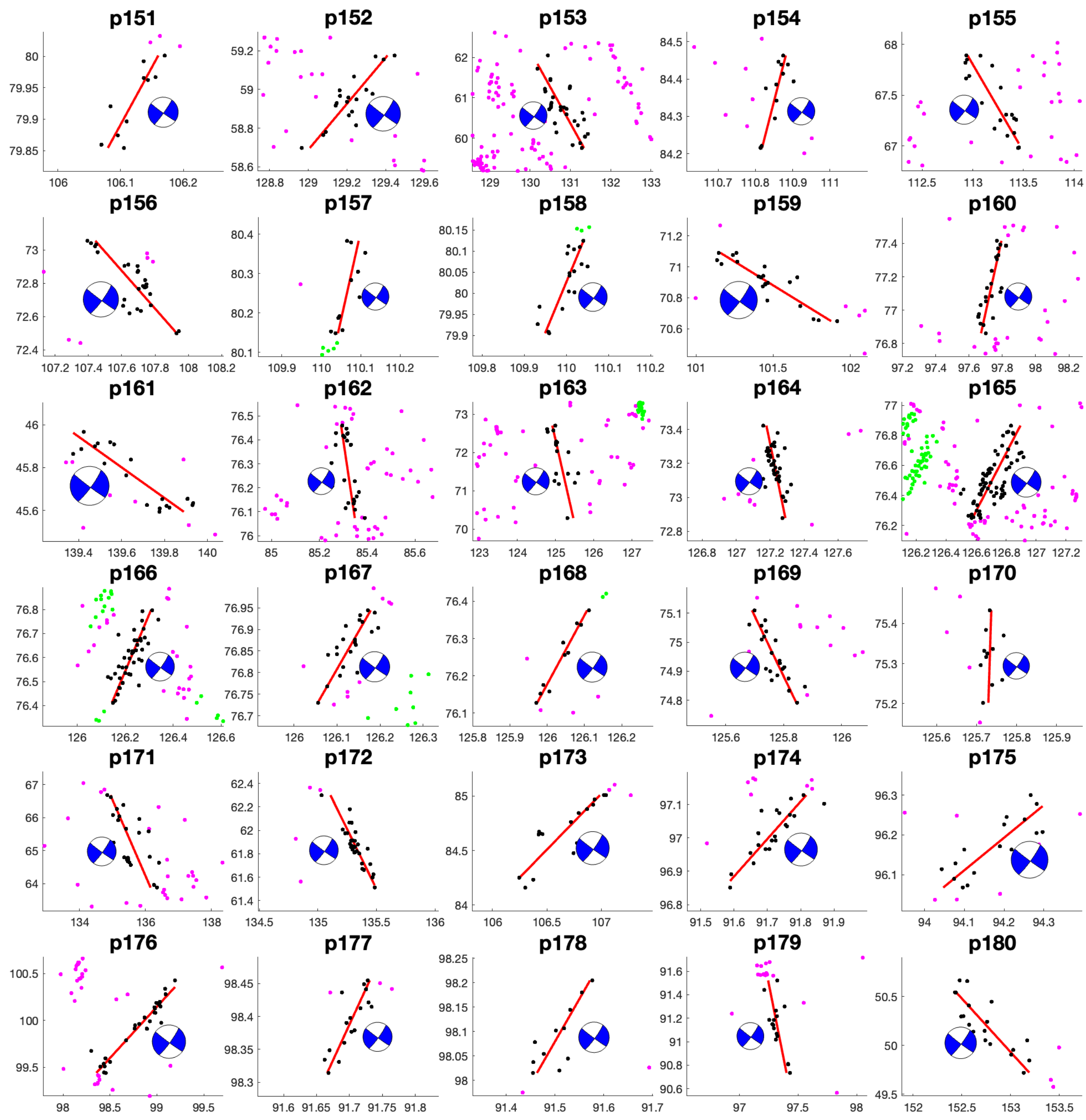

Figure S10. Close-up views of selected quasi-linear clusters. Each panel shows a quasi-linear cluster (black dots), along with a composite focal mechanism (blue beach ball). Solid red line denotes a best-fit line segment. Magenta dots denote background seismicity. Green dots denote other selected quasi-linear clusters.

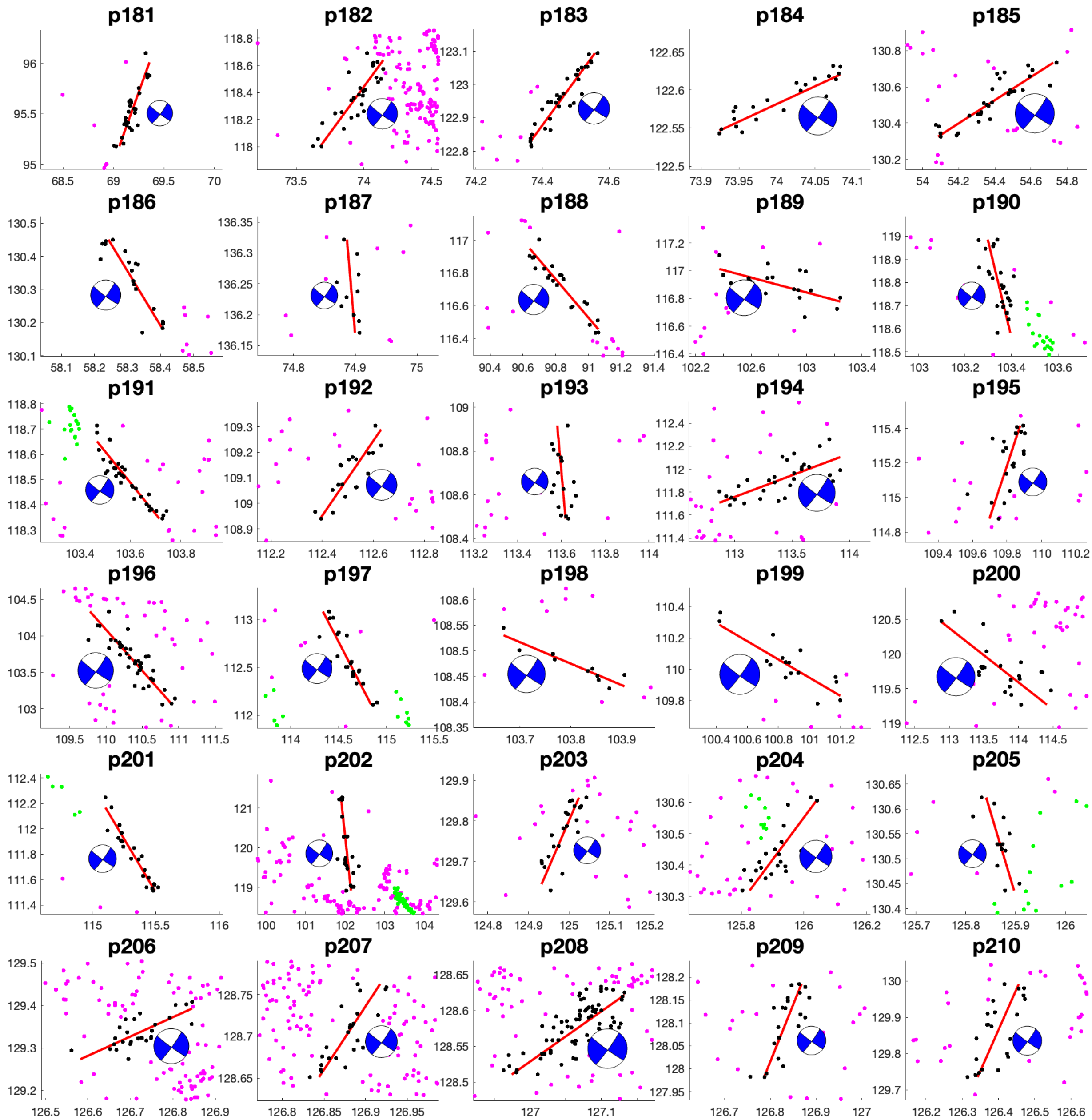

Figure S11. Close-up views of selected quasi-linear clusters. Each panel shows a quasi-linear cluster (black dots), along with a composite focal mechanism (blue beach ball). Solid red line denotes a best-fit line segment. Magenta dots denote background seismicity. Green dots denote other selected quasi-linear clusters.

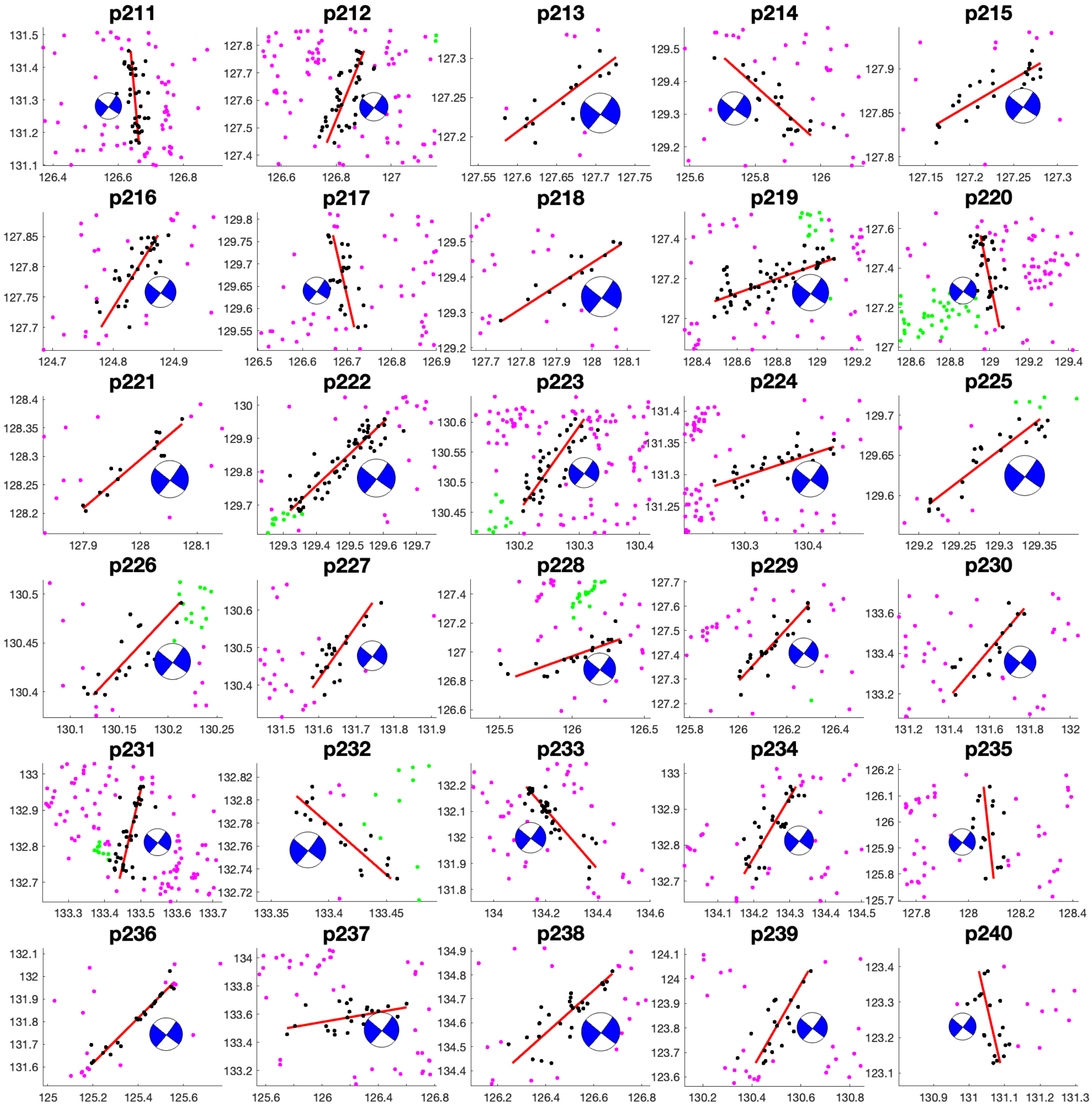

Figure S12. Close-up views of selected quasi-linear clusters. Each panel shows a quasi-linear cluster (black dots), along with a composite focal mechanism (blue beach ball). Solid red line denotes a best-fit line segment. Magenta dots denote background seismicity. Green dots denote other selected quasi-linear clusters.

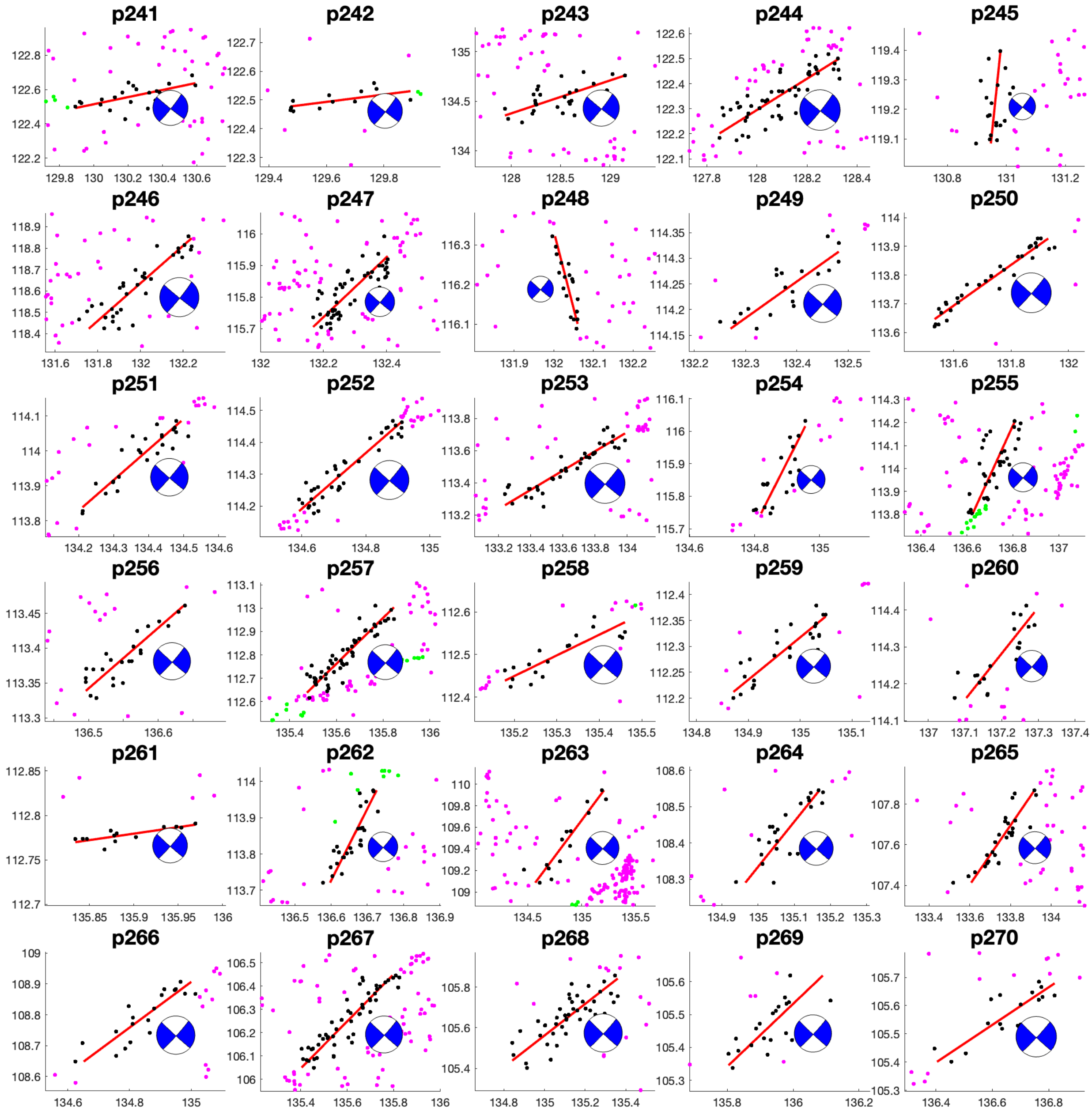

Figure S13. Close-up views of selected quasi-linear clusters. Each panel shows a quasi-linear cluster (black dots), along with a composite focal mechanism (blue beach ball). Solid red line denotes a best-fit line segment. Magenta dots denote background seismicity. Green dots denote other selected quasi-linear clusters.

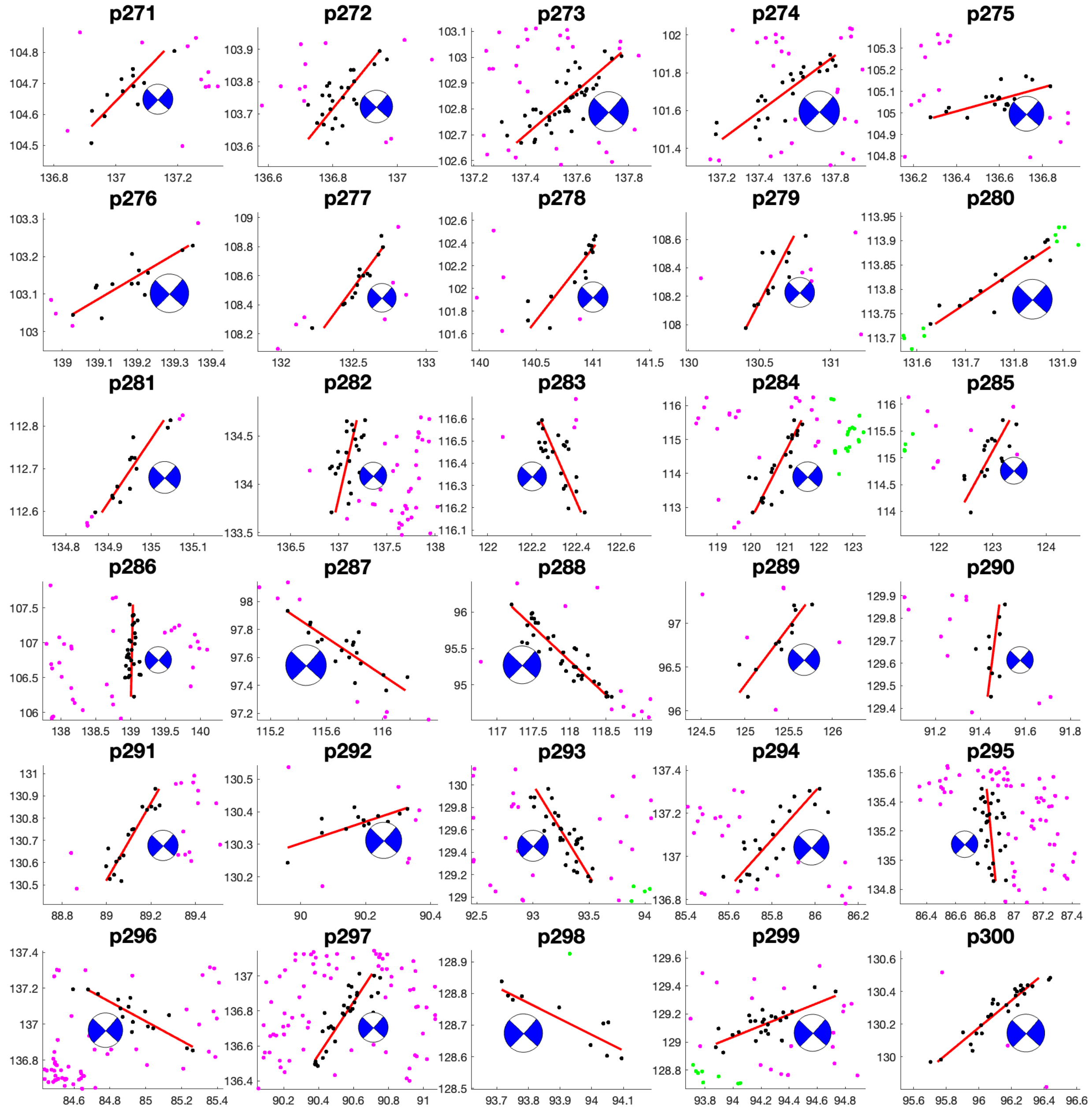

Figure S14. Close-up views of selected quasi-linear clusters. Each panel shows a quasi-linear cluster (black dots), along with a composite focal mechanism (blue beach ball). Solid red line denotes a best-fit line segment. Magenta dots denote background seismicity. Green dots denote other selected quasi-linear clusters.

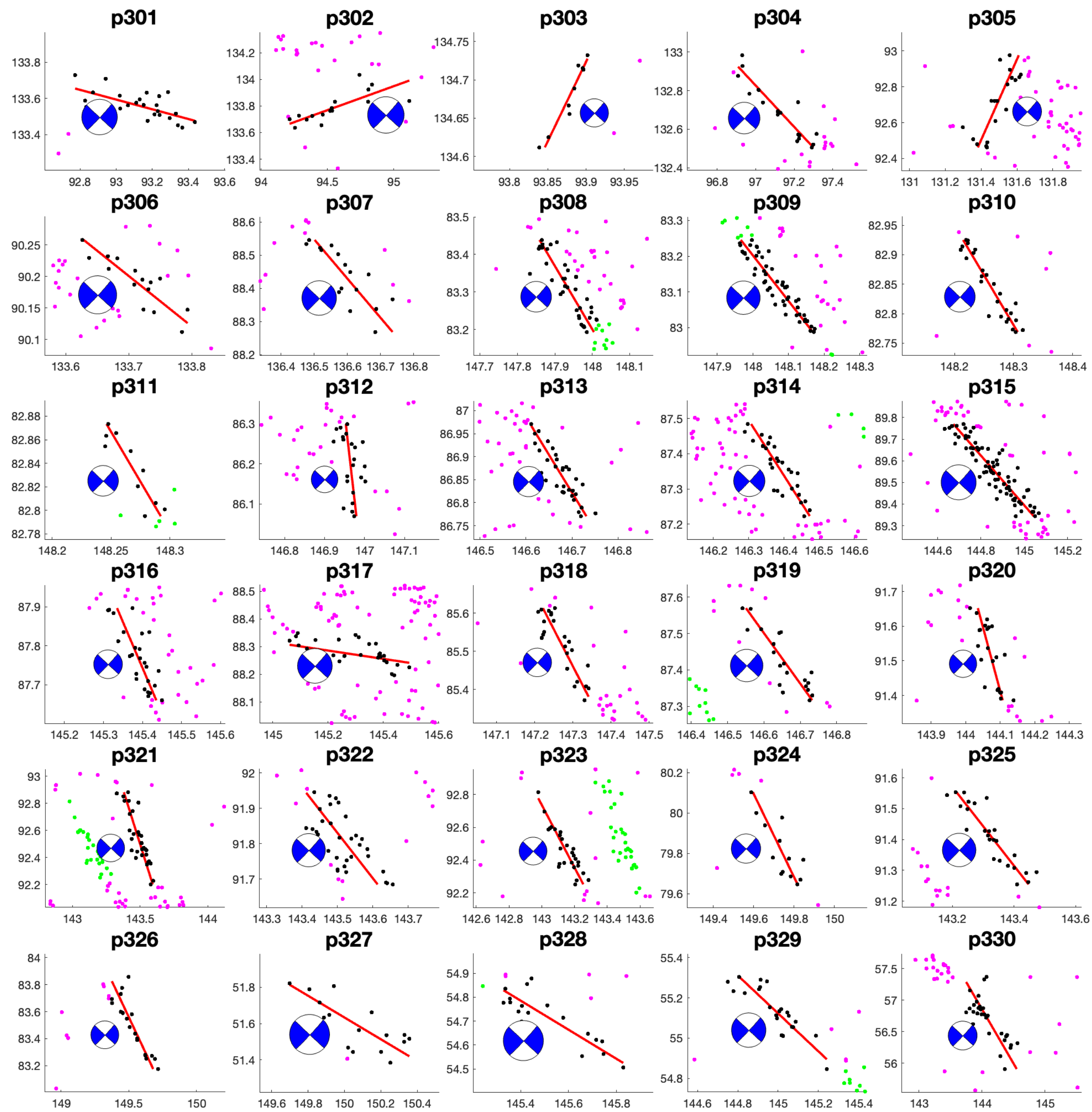

Figure S15. Close-up views of selected quasi-linear clusters. Each panel shows a quasi-linear cluster (black dots), along with a composite focal mechanism (blue beach ball). Solid red line denotes a best-fit line segment. Magenta dots denote background seismicity. Green dots denote other selected quasi-linear clusters.

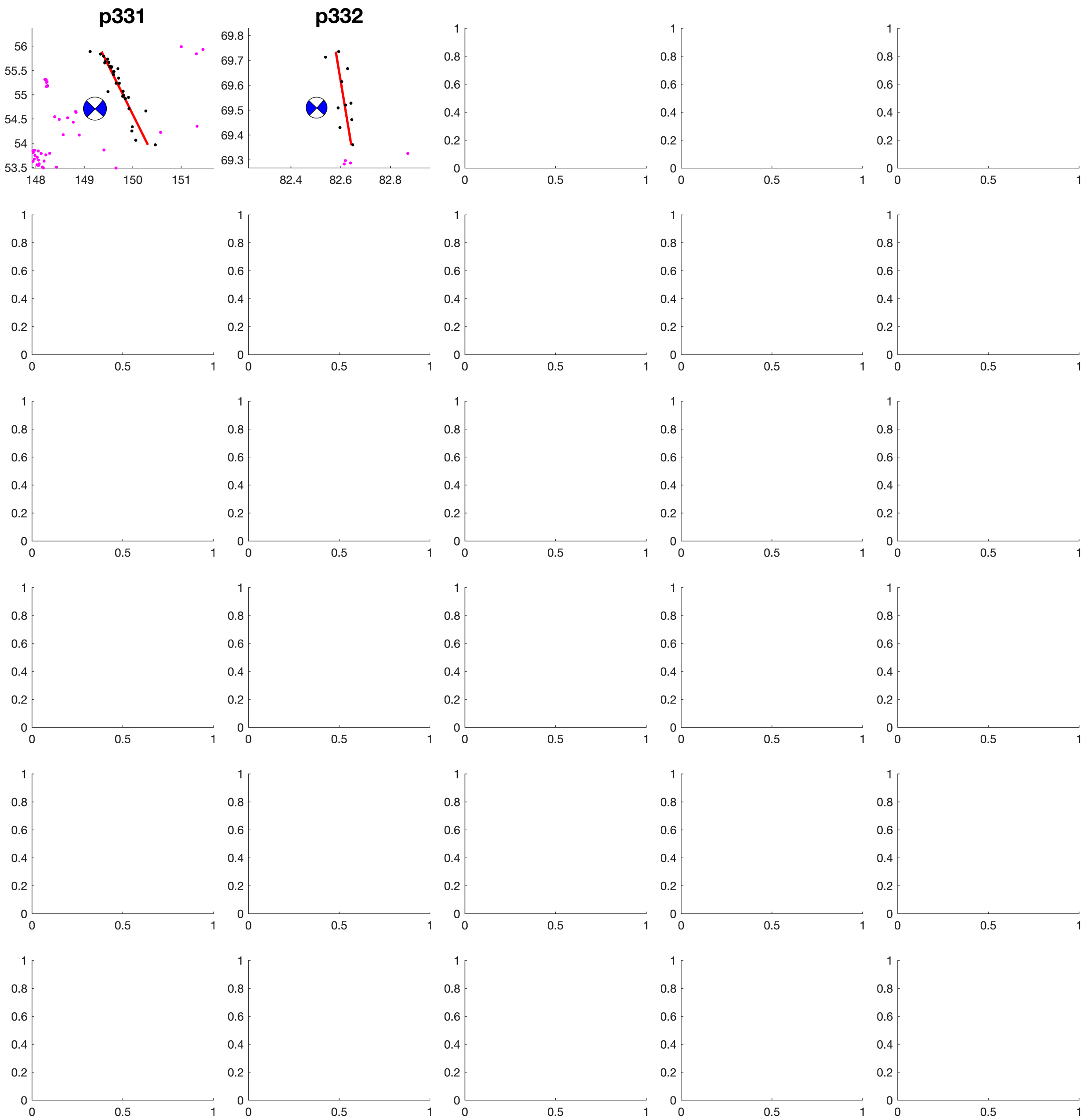

Figure S16. Close-up views of selected quasi-linear clusters. Each panel shows a quasi-linear cluster (black dots), along with a composite focal mechanism (blue beach ball). Solid red line denotes a best-fit line segment. Magenta dots denote background seismicity. Green dots denote other selected quasi-linear clusters.